Role of ocean and atmosphere variability in scale-dependent thermodynamic air-sea interactions

Lucas C. Laurindo[1,2], R. Justin Small[1,2], LuAnne Thompson[3], Leo Siqueira[4], Frank O. Bryan[2], Ping Chang[1,5,6], Gokhan Danabasoglu[1,2], Igor V. Kamenkovich[4], Ben P. Kirtman[4], Hong Wang[1,7,8], and Shaoqing Zhang[1,7,8]

[1]International Laboratory for High-Resolution Earth System Prediction (iHESP), Texas A&M University, College Station, TX, USA.
[2]National Center for Atmospheric Research, Boulder, Colorado, USA.
[3]School of Oceanography, University of Washington, Seattle, WA, USA.
[4]Rosenstiel School of Marine & Atmospheric Science, University of Miami, Miami, USA.
[5]Department of Oceanography, Texas A&M University, College Station, TX, USA.
[6]Department of Atmospheric Sciences, Texas A&M University, College Station, TX, USA.
[7]Laboratory for Ocean Dynamics and Climate, Qingdao Pilot National Laboratory for Marine Science and Technology, Qingdao, China.
[8]Key Laboratory of Physical Oceanography, the College of Oceanic and Atmospheric Sciences, the Institute for Advanced Ocean Study & Center for Deep Ocean Multispheres and Earth System (DOMES), Ocean University of China, Qingdao, China.

Key Points:

- We use spectral methods to examine the role of oceanic and atmospheric processes in Pacific SST and turbulent heat flux variability.
- At mid-latitudes, the atmosphere controls variability with scales larger than 2000 km while ocean processes dominate at smaller scales.
- Ocean phenomena drive a red spectrum SST response similar to that induced by the atmosphere, which is mirrored by the turbulent fluxes.

Corresponding author: Lucas C. Laurindo, `laurindo@ucar.edu`

Abstract

This study investigates the influence of oceanic and atmospheric processes in extratropical thermodynamic air-sea interactions resolved by satellite observations (OBS) and by two climate model simulations run with eddy-resolving high-resolution (HR) and eddy-parameterized low-resolution (LR) ocean components. Here, spectral methods are used to characterize the sea surface temperature (SST) and turbulent heat flux (THF) variability and co-variability over scales between 50-10000 km and 60 days-80 years in the Pacific Ocean. The relative roles of the ocean and atmosphere are interpreted using a stochastic upper-ocean temperature evolution model forced by noise terms representing intrinsic variability in each medium, defined using climate model data to produce realistic rather than white spectral power density distributions. The analysis of all datasets shows that the atmosphere dominates the SST and THF variability over zonal wavelengths larger than ∼2000-2500 km. In HR and OBS, ocean processes dominate the variability of both quantities at scales smaller than the atmospheric first internal Rossby radius of deformation (R_1, ∼600-2000 km) due to a substantial ocean forcing coinciding with a weaker atmospheric modulation of THF (and consequently of SST) than at larger scales. The ocean-driven variability also shows a surprising temporal persistence, from intraseasonal to multidecadal, reflecting a red spectrum response to ocean forcing similar to that induced by atmospheric forcing. Such features are virtually absent in LR due to a weaker ocean forcing relative to HR.

Plain Language Summary

This study investigates the importance of atmospheric processes (weather) and ocean currents in driving variations in sea surface temperature (SST) and the air-sea heat exchange at mid-latitudes. Our analysis uses satellite observations, a high-resolution (HR) climate model that resolves ocean currents with dimensions of tens of km, and a low-resolution model (LR) that can only simulate ocean currents with hundreds of km in size. We specifically examine how variable SST and the heat exchange are in each of these datasets at horizontal scales between 50 and 10000 km and time scales from two months to eighty years in the Pacific Ocean. Using a simple mathematical model to interpret the results, we find that variability at scales larger than 2000 km is driven predominantly by weather. At smaller scales, SST and heat exchange are more variable in HR than in LR and agree better with satellite observations. We also find that ocean processes drive variability in SST with time scales ranging from two months to several decades, similar to those caused by weather, which induces slow variations in the air-sea heat exchange.

1 Introduction

Interactions between the atmosphere and oceans largely determine the Earth's climate, and the physical mechanisms controlling these interactions are scale-dependent. In midlatitudes, at large spatial scales ($\mathcal{O}[10^3$ km]) the atmosphere modulates the surface turbulent heat fluxes (THF) via the prevailing winds and the advection of humidity and air temperature by synoptic weather systems, producing slow fluctuations in sea surface temperature (SST) that lag the heat flux signal over time scales of several weeks or longer (e.g., Barsugli & Battisti, 1998; Frankignoul et al., 1998; von Storch, 2000; Okumura et al., 2001; Xie, 2004; Small et al., 2019). At ocean mesoscales ($\mathcal{O}[10^1$–10^2 km]), ocean currents can create SST anomalies that are large and persistent such that they induce anomalous surface heat fluxes. The response in THF is forced by air-sea temperature and humidity differences arising when an air parcel moves over mesoscale SST features, and is proportional to the magnitude of the underlying SST signal (e.g., Wu et al., 2006; Villas Bôas et al., 2015; Putrasahan et al., 2017; Bishop et al., 2017; Small et al., 2019). While the large-scale regime is traditionally considered important in climate dynamics, there is growing evidence that mesoscale air-sea coupling can influence oceanic and atmospheric variability (e.g., Chelton et al., 2004; O'Neill et al., 2010; Frenger et al., 2013; Putrasahan et al., 2013; Gaube et al., 2015; Ma et al., 2015, 2016, 2017; Putrasahan et al., 2017; Laurindo et al., 2019) and play a key role in weather and climate (e.g., Minobe et al., 2008; Siqueira & Kirtman, 2016; Ma et al., 2015, 2017; Kirtman et al., 2017; Chang et al., 2020; Siqueira et al., 2021).

Despite the importance of mesoscale air-sea interactions revealed by literature, the physical mechanisms that allow them to prevail over the large-scale regime remain poorly understood. To investigate these mechanisms, this work uses spectral methods to characterize the SST and THF variability and co-variability resolved by satellite observations and climate model simulations over scales between 50-10000 km and 60 days-80 years in the models and up to nineteen years for observations. The roles of oceanic and atmospheric processes in the obtained spectra are then interpreted using an idealized stochastic climate model. The presented analysis focuses on the Pacific Ocean, although similar results and conclusions are also obtained for the Indian and Atlantic basins.

Several previous studies used stochastic climate models to analyze the basic effects of the extratropical thermodynamic air-sea coupling (e.g., Wu et al., 2006; O'Reilly et al., 2016; Bishop et al., 2017; Sun & Wu, 2021). These idealized models represent the mechanisms in the ocean and atmosphere that generate variability in the upper-ocean temperature as stochastic (i.e., random) processes, and indicate that linear, time-domain relationships between SST and THF can be used to infer the local dominance of either

ocean- or atmosphere-driven variability in both quantities. Specifically, when the atmosphere forcing signal is strong, solutions derived from the stochastic formulations produce negative correlations between the SST rate of change (known as the SST *tendency*) and THF at lag zero, concurrent with lead-lag SST/THF correlations. In turn, when the ocean forcing term is strong (and defining THF as being positive when out of the ocean), positive correlations arise between SST and THF at lag zero, while SST tendency and THF are related in a lagged fashion (c.f. Fig. 1 of Bishop et al., 2017).

Consistent with the conclusions drawn from idealized formulations, fully-coupled climate model simulations reproduce linear relationships characteristic of atmosphere- or ocean-driven variability depending on the resolution of their ocean components. When the resolution is insufficient to resolve mesoscale ocean eddies, linear SST/THF relationships suggest that the variability is primarily driven by the atmosphere over much of the extratropics. In contrast, horizontal ocean resolutions sufficiently refined to allow eddy formation and evolution significantly enhance the mesoscale current variability (Sérazin et al., 2015, 2018; Constantinou & Hogg, 2021), which increases the local upper-ocean heat convergence anomalies that in turn lead to larger SST variability, most prominently in strong current systems such as the seaward extensions of western boundary currents and the Antarctic Circumpolar Current (ACC) (Putrasahan et al., 2017; Sérazin et al., 2017; Small et al., 2020; Constantinou & Hogg, 2021). The SST variability at these regions is positively correlated with THF (Kirtman et al., 2012; Ma et al., 2016; Roberts et al., 2016; Chang et al., 2020), a characteristic that is also present in satellite estimates (Villas Bôas et al., 2015; Ma et al., 2016; Bishop et al., 2017; Small et al., 2019), suggesting that the mesocale air-sea coupling regime is dominant there.

Recently, several studies examined the spatial and temporal scales where ocean dynamics can influence the extratropical SST variability and consequently impact THF. For instance, the analysis of satellite data indicate that ocean processes dominate the variability of both quantities over spatial scales smaller than ∼500-700 km and up to interannual timescales at most latitudes (Bishop et al., 2017; Small et al., 2019). Historical ship-based observations show that SST fluctuations of the Atlantic Multidecadal Variability (AMV) – a climate mode in SST thought to be driven by the Atlantic Meridional Overturning Circulation (AMOC, Buckley et al., 2015; R. Zhang et al., 2019) – are positively correlated with THF in the subpolar North Atlantic (Gulev et al., 2013; O'Reilly et al., 2016). In support of these observational findings, eddy-resolving simulations indicate that mesoscale currents enhance the variability in upper-ocean heat content and SST over spatial scales smaller than about 1000 km and timescales up to several decades in regions with strong extratropical current systems (Sérazin et al., 2017, 2018; Constanti-

nou & Hogg, 2021). Fully-coupled simulations show similar results, and further indicate that the THF variability is also enhanced (Small et al., 2020; Chang et al., 2020). The importance of ocean phenomena on driving changes in SST and THF over intraseasonal to decadal timescales was also revealed in an eddy-resolving simulation of an idealized western boundary current system (Martin et al., 2021) and by the Estimating the Circulation and Climate of the Ocean v4 (ECCO) ocean state estimate in the extratropics (Patrizio & Thompson, 2021a, 2021b).

The results from these previous studies indicate that ocean processes can overcome the large-scale, atmosphere-driven modulation of THF and SST over spatial and temporal scales that are larger and longer (potentially much more so) than that of individual mesoscale eddies. They also indicate that, although the main differences between the large-scale and mesoscale air-sea coupling regimes are well established, the spatial and temporal scales where each regime prevails are still not well characterized, nor are the physical mechanisms that give rise to their scale dependence. This work addresses these gaps. The main hypotheses are that the relative importance of the ocean processes driving the SST and THF variability

(a) Increases toward the ocean mesoscales due to a strong intrinsic ocean variability coinciding with a weaker atmospheric modulation of THF (and consequently of SST) than at larger spatial scales, owing to the weaker variability of atmospheric processes at smaller spatial scales; and

(b) Increase toward longer timescales, because ocean processes induce low-frequency SST fluctuations via a mechanism similar to that caused by atmospheric stochastic forcing (Hasselmann, 1976; Frankignoul & Hasselmann, 1977) where the large heat capacity of the upper-ocean integrates the forcing noise to produce a red spectrum response in SST.

The present study tests these hypotheses by examining the SST and THF power spectra and cross-spectral statistics resolved by a satellite product and by fully-coupled climate model simulations run with eddy-resolving and eddy-parameterized horizontal ocean resolutions. The obtained spectral quantities are interpreted using a stochastic model of air-sea interactions forced by noise terms representing the action of atmospheric and oceanic processes. Here, the noise terms are defined with realistic variance distributions as a function of frequency and zonal wavenumber taken from the climate model simulations. This approach contrasts with that typically adopted in the literature, where the forcing terms are represented as randomly-generated white noise signals with variances

approximately constant across all scales (e.g., Frankignoul et al., 1998; von Storch, 2000; Wu et al., 2006; Bishop et al., 2017; Sun & Wu, 2021).

The remainder of this paper is organized as follows: Sec. 2 describes the satellite and climate model datasets used (2.1), the spectral data analysis methods (2.2), and the methods involved in the stochastic climate model analysis (2.3). Sec. 3 examines the spectra predicted by the stochastic model and how they compare with corresponding estimates obtained using white noise forcing. Sec. 4 first briefly describes the global SST and THF variance distribution resolved by the satellite and model datasets (4.1), then presents the power spectral densities and cross-spectral statistics computed using SST and THF data as well as corresponding results predicted using the stochastic model (4.2). Sec. 5 discusses the results in light of the existing literature, and Sec. 6 summarizes this study and its conclusions.

2 Methods

2.1 Data description

2.1.1 J-OFURO3 observational product:

Observational estimates of SST and THF are from the Japanese Ocean Flux Data Sets with Use of Remote-Sensing Observations version 3 (J-OFURO3, Tomita et al., 2019). Briefly, the J-OFURO3 dataset gives estimates of THF (defined as positive upwards) and its components. THF is estimated using the COARE 3.0 bulk formulations (Fairall et al., 2003), whose variables are retrieved from various satellite data sources except for 2-m height temperature, which is from an atmospheric reanalysis. In turn, SST is the daily median of values taken from multiple satellite missions and regularly-gridded SST products, an approach designed to provide a robust SST estimate while minimizing uncertainties intrinsic to any single data source (Kubota et al., 2002; Tomita et al., 2019). The J-OFURO3 data (OBS) used in this study was produced at a $0.25° \times 0.25° \times$ 1-month resolution for January 1988 to December 2013.

2.1.2 CESM1.3 climate model simulations:

This study uses climate simulations generated with the Community Earth System Model version 1.3 (CESM1.3, Meehl et al., 2019; S. Zhang et al., 2020) by the International Laboratory for High-Resolution Earth System Prediction (iHESP, Chang et al., 2020). The CESM1.3 is a global climate model composed of the Community Atmosphere Model version 5 (Neale et al., 2012), the Parallel Ocean Program version 2 (Smith et al., 2010; Danabasoglu et al., 2012), the Community Ice Code version 4 (Hunke & Lipscomb,

198 2010), and the Community Land Model version 4 (Lawrence et al., 2011). The model
199 components exchange state information and fluxes via the CESM Coupler 7, which com-
200 putes the fluxes at the air-sea interface using the Large and Yeager (2004) bulk param-
201 eterizations.

202 Outputs from two iHESP CESM1.3 preindustrial control simulations are analyzed,
203 run at contrasting horizontal resolutions in the ocean and atmosphere. The first (low-
204 resolution, LR) uses a nominal 1° horizontal resolution in both model components that
205 cannot resolve mesoscale ocean eddies, whose effects are parameterized (Gent & McWilliams,
206 1990). The second (high-resolution, HR) is configured with a nominal 0.25° horizontal
207 resolution in the atmosphere and 0.1° in the ocean, which is eddy-resolving in the ocean
208 except at high latitudes. Both the HR and LR experiments use an atmospheric CO_2 con-
209 centration fixed at 1850 levels and are integrated for 500 years (Chang et al., 2020).

210 The HR and LR data used in this work are monthly global fields of SST, THF, and
211 2-m height humidity, and three-dimensional monthly global fields of ocean heat flux con-
212 vergence (OHFC), computed using horizontal and vertical components of the heat flux,
213 that are vertically-integrated for the upper 50-m of the water column. The 50-m inte-
214 gration level is chosen for consistency with the stochastic climate model formulation de-
215 scribed in Sec. 2.3. All quantities obtained from LR (HR) are mapped onto a regular
216 $1° \times 1°$ ($0.25° \times 0.25°$) spatial grid and are retrieved for the simulation years 21-500
217 (338-500) based on their availability in the model output files.

218 **2.2 Spectral analysis**

219 This work examines the power spectra of SST and THF and their cross-spectra in
220 HR, LR, and OBS as a function of frequency and zonal wavenumber. This spectral anal-
221 ysis is similar to that described in Laurindo et al. (2019) for SST and 10-m wind speed.
222 More specifically, it examines spectra varying as a function of both zonal wavenumber
223 and frequency (k and ω, respectively) computed from zonal-temporal (x, t) diagrams of
224 the considered quantities at every 1° (0.25°) latitude in LR (HR and OBS) between 55°S
225 and 60°N in the Pacific Ocean. This analysis is performed within a Pacific basin mask
226 (Fig. 1h) that excludes regions shallower than 1000-m around the continental shelves to
227 avoid the influence of coastal processes. The mask also ignores small islands at the basin's
228 interior, whose gaps in the data are filled using linear interpolation.

229 Zonal-temporal diagrams of SST and THF obtained at each latitude increment are
230 demeaned in both (x, t) directions, and the time series at each grid point is further de-
231 trended and deseasonalised using annual and semiannual harmonics. The processed zonal-

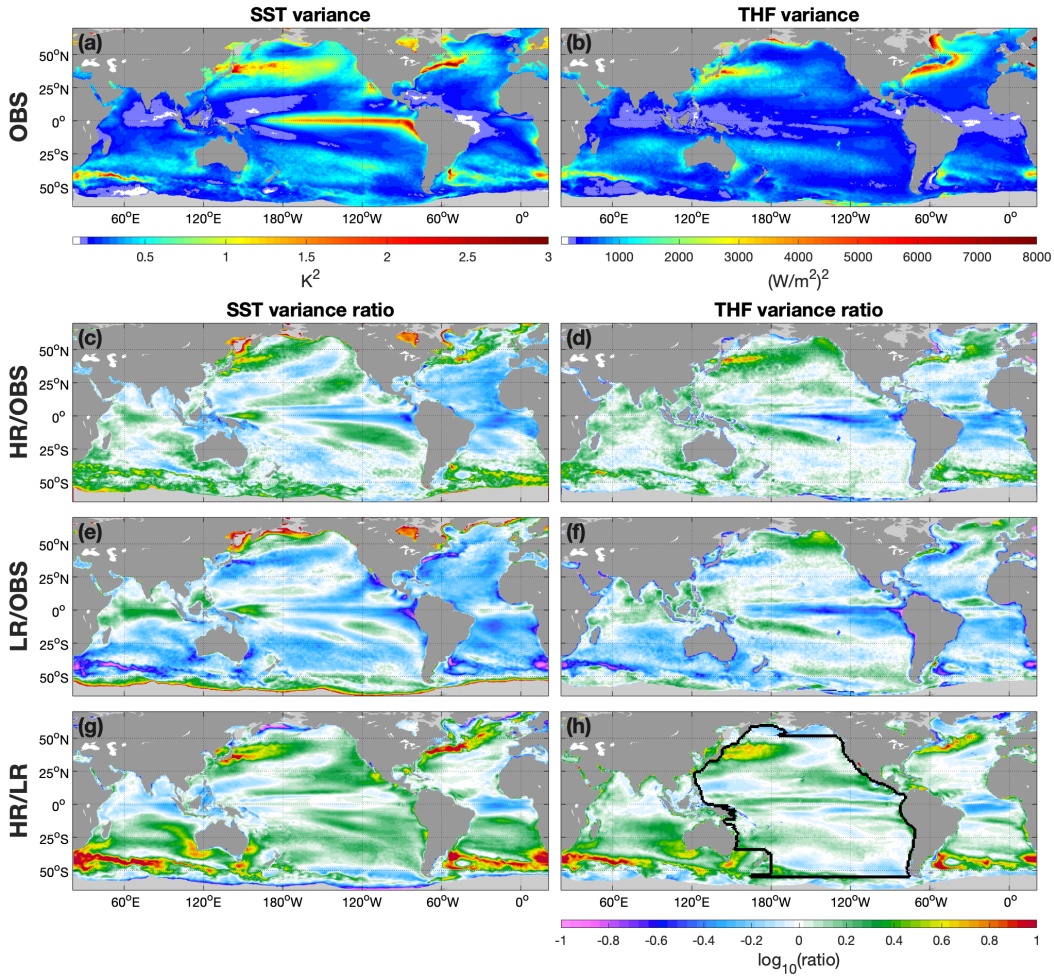

Figure 1. Global maps of the SST and THF variances resolved by the J-OFURO3 satellite product (OBS, panels a and b, respectively), and the ratios of the corresponding variances resolved by the HR (c-d) and LR (e-f) to those of respective OBS. Panels (g) and (h) show the ratios between the variances resolved in HR and LR. The black contour in (h) delineates the basin mask for the Pacific Ocean used for the zonal-temporal spectral analysis.

temporal diagrams of SST $[T(x,t)]$ and THF $[Q(x,t)]$ are then subdivided into 80-year segments for HR and LR, and into 19-year segments for OBS, with a 50% temporal overlap. The resulting data segments are selected within 4° meridional bands centered at each grid point of the latitudinal axis, forming ensembles containing multiple realizations of $T(x,t)$ and $Q(x,t)$ (48 for HR, 44 for LR, and 34 for OBS), that are used to compute the spectral functions at each latitude.

Following Bendat and Piersol (1986), the power spectral density functions (also known as autospectral density functions) of $T(x,t)$ and $Q(x,t)$ are defined as:

$$G_{TT}(k,\omega) = \frac{2}{l_k l_\omega} \left\langle |\tilde{T}(k,\omega)|^2 \right\rangle, \text{ and} \tag{1}$$

$$G_{QQ}(k,\omega) = \frac{2}{l_k l_\omega} \left\langle |\tilde{Q}(k,\omega)|^2 \right\rangle, \tag{2}$$

where the tilde denotes a two-dimensional Fourier transform to the k and ω domains, l_k (l_ω) is the length of $\tilde{T}$ and $\tilde{Q}$ in the zonal wavenumber (frequency) domain, and the brackets represent ensemble-averages over the $|\tilde{T}(k,\omega)|^2$ and $|\tilde{Q}(k,\omega)|^2$ realizations.

Similarly, the cross-spectral density function between $T(x,t)$ and $Q(x,t)$ is given by:

$$G_{TQ}(k,\omega) = \frac{2}{l_k l_\omega} \left\langle \tilde{T}^*(k,\omega)\tilde{Q}(k,\omega) \right\rangle, \tag{3}$$

where the asterisk denotes complex conjugation.

The spectral functions are computed as functions of both k and ω. The results are then integrated in frequency domain to obtain estimates as a function of zonal wavenumber and latitude, and separately integrated in the zonal wavenumber domain to obtain estimates as a function of frequency and latitude. The integrated estimates are also used to compute the magnitude-squared coherence γ^2_{TQ} as:

$$\gamma^2_{TQ} = \frac{|G_{TQ}|^2}{G_{TT}G_{QQ}}, \tag{4}$$

where $G_{TQ} = |G_{TQ}|e^{-i\theta_{TQ}}$, with θ_{TQ} (known as phase factor) describing the phase relationship between the sinusoidal components of $\tilde{T}$ and $\tilde{Q}$. γ^2_{TQ} varies between zero and one, reflecting the fraction of the variance of Q that can be explained by T for each spectral coordinate.

2.3 Stochastic upper-ocean temperature anomaly model

2.3.1 Model description:

This work uses a stochastic model for the upper-ocean temperature evolution proposed by Frankignoul et al. (1998) (hereafter FCL98) to guide the physical interpretation of the spectral quantities computed for SST and THF (Sec. 2.2).

The FCL98 formulation can be written as:

$$\rho_0 c_p h \frac{\partial T}{\partial t} = N_a + N_m - (\lambda_q + \lambda_0)T, \tag{5}$$

where T is the temperature of a well-mixed upper-ocean layer of thickness h, density ρ_0, and specific heat c_p. N_a represents the stochastic forcing of the turbulent heat fluxes by intrinsic atmospheric variability, and N_m denotes the forcing by other processes, identified in FCL98 as primarily representing the action of wind stress variability. Lastly, λ_q and λ_0 are feedback factors responsible for damping the temperature anomalies, the former associated with THF and the latter to terms unrelated to the air-sea fluxes, such as radiative cooling and turbulent mixing.

In this work, Eq. (5) is modified by attributing the origin of the N_m stochastic forcing term to internal ocean variability (thus renaming it N_o), the origin of the λ_0 feedback factor solely to radiative cooling (being renamed λ_r), and by considering that the stochastic forcing term N_a represents stochastic variability in the near-surface atmospheric temperature rather than in THF, approach similar to that used in Barsugli and Battisti (1998). With these, Eq. (5) becomes:

$$\frac{\partial T}{\partial t} = -\alpha\,(T - N_a) - \beta T + \nu N_o, \tag{6}$$

where $\nu = 1/(\rho_0 c_p h)$, $\alpha = \lambda_q \nu$, and $\beta = \lambda_r \nu$. Here, THF is defined as $Q = \lambda_q(T - N_a)$, with positive values denoting fluxes out of the ocean. The values of the coefficients α, β, ν, and λ_q are computed for a $h = 50$-m thick ocean layer as described in Barsugli and Battisti (1998), and are listed in Table 1.

The stochastic model defined in Eq. (6) was developed for mid-latitudes and is unable to represent important air-sea coupling mechanisms at work within the tropics, such as the Bjerknes feedback and the Wind-Evaporation-Sea Surface Temperature (WES) feedback (e.g., Mahajan et al., 2009). For this reason, the present work uses Eq. (6) to support the interpretation of spectral estimates obtained at latitudes poleward of 15°. Other limitations are discussed in Sec. 5.3.

Table 1. Values of the FCL98 model parameters [Eqs. (6)-(9)].

Parameter	Value
ρ_0	1025.0 kg m^{-3}
c_p	3900.0 J kg^{-1} K^{-1}
h	50.0 m
λ_q	23.4 W m^{-2} K^{-1}
λ_r	1.3 W m^{-2} K^{-1}

The stochastic model defined by Eq. (6) is Fourier transformed to zonal wavenumber and frequency domains (k, ω) and used to obtain analytical expressions for G_{TT}, G_{QQ}, and G_{TQ}, given by:

$$G_{TT} = \frac{2}{l_k l_\omega}\left[\frac{\nu^2\langle|\tilde{N}_o|^2\rangle + \alpha^2\langle|\tilde{N}_a|^2\rangle}{4\pi^2\omega^2 + (\alpha+\beta)^2}\right], \tag{7}$$

$$G_{QQ} = \frac{2\lambda_q^2}{l_k l_\omega}\left\{\frac{\nu^2\langle|\tilde{N}_o|^2\rangle + [4\pi^2\omega^2 + \beta^2]\langle|\tilde{N}_a|^2\rangle}{4\pi^2\omega^2 + (\alpha+\beta)^2}\right\}, \text{ and} \tag{8}$$

$$G_{TQ} = \frac{2\lambda_q}{l_k l_\omega}\left\{\frac{\nu^2\langle|\tilde{N}_o|^2\rangle + \alpha[i2\pi\omega - \beta]\langle|\tilde{N}_a|^2\rangle}{4\pi^2\omega^2 + (\alpha+\beta)^2}\right\}. \tag{9}$$

where $\tilde{N}_o$ and $\tilde{N}_a$ are Fourier transformed stochastic noise terms.

Cross-terms between $\tilde{N}_o$ and $\tilde{N}_a$ are small by design assuming that intrinsic variability in the ocean and the atmosphere are unrelated to each other, and are thus omitted in Eqs. (7)-(9). The analytical expressions shown in Eqs. (7)-(9) are also substituted in Eq. (4) to obtain stochastic model estimates of coherence (γ^2_{TQ}) and phase factor (θ_{TQ}).

2.3.2 Calculating the $\langle|\tilde{N}_o|^2\rangle$ and $\langle|\tilde{N}_a|^2\rangle$ forcing spectra:

In the context of air-sea interactions, previous studies have defined stochastic models varying solely as a function of time, representing the forcing by oceanic and atmospheric processes as stochastic signals with a "white" spectral power density in frequency space – i.e., with approximately the same variance (power) at every frequency. While observations support the white noise assumption in frequency space (e.g., Frankignoul et al., 1998; Patrizio & Thompson, 2021b), they also show that the spectra of intrinsic atmospheric and oceanic motions are "red" in wavenumber space, with more variance at larger wavelengths (e.g., Nastrom & Gage, 1985; Ducet et al., 2000). The variance distribution in wavenumber space also differ between each medium, likely reflecting the

distinct intrinsic scales of synoptic weather systems and mesoscale ocean eddies. The present work hypothesizes that these distinct variance distributions in time and space can give rise to the spatial scale dependence of thermodynamic air-sea interactions revealed by recent assessments (Bishop et al., 2017; Laurindo et al., 2019; Small et al., 2019, 2020). To test this hypothesis, data from HR and LR are used to attribute realistic variance distributions in zonal wavenumber and frequency domains to the $\langle|\tilde{N}_o|^2\rangle$ and $\langle|\tilde{N}_a|^2\rangle$ forcing spectra in Eqs. (7)-(9).

More specifically, 2-m height specific humidity is used to define $\langle|\tilde{N}_a|^2\rangle$ because (a) this quantity is related to the latent turbulent heat flux bulk formulation (Fairall et al., 2003; Large & Yeager, 2004); (b) the latent heat fluxes are usually larger than the sensible heat fluxes; and (c) time-domain correlations and coherence estimates show that the 2-m height specific humidity variability is weakly related to (and thus largely independent from) mesoscale SST anomalies in most oceanic regions (not shown), suggesting that atmospheric processes predominantly drives its variability. In turn, OHFC is used to define $\langle|\tilde{N}_o|^2\rangle$ considering that it corresponds to the main driver of mesoscale SST variability (Putrasahan et al., 2017; Small et al., 2020).

To compute $\langle|\tilde{N}_o|^2\rangle$ and $\langle|\tilde{N}_a|^2\rangle$, zonal-temporal diagrams of OHFC and 2-m height humidity data from HR and LR are selected at each latitude within the Pacific basin as defined by the mask (Fig. 1h). These diagrams are first normalized by their respective standard deviations to render their variances equal to one, and then undergo the the same processing steps applied to SST and THF data for obtaining their power spectra (Sec. 2.2), here producing $\langle|\tilde{N}_o|^2\rangle$ and $\langle|\tilde{N}_a|^2\rangle$. Finally, to approximate the stochastic model solutions to the G_{TT}, G_{QQ}, γ^2_{TQ}, and $|\theta_{TQ}|$ spectra resolved by HR and LR, the variances that $\langle|\tilde{N}_o|^2\rangle$ and $\langle|\tilde{N}_a|^2\rangle$ should integrate to (σ_o^2 and σ_a^2) are estimated using a least-squares approach described in Appendix A.

3 Analysis of the stochastic model solutions

This Section contrasts $\langle|\tilde{N}_o|^2\rangle$ and $\langle|\tilde{N}_a|^2\rangle$ forcing spectra defined using HR and LR data (hereafter referred to as geophysical noise) with those defined using with white noise, and compares stochastic model estimates of G_{TT}, G_{QQ}, γ^2_{TQ}, and $|\theta_{TQ}|$ computed using each type of forcing separately. Here, estimates computed using geophysical noise are illustrated for HR and 40°S in the Pacific. This latitude is chosen to demonstrate characteristics that are representative of the extratropics.

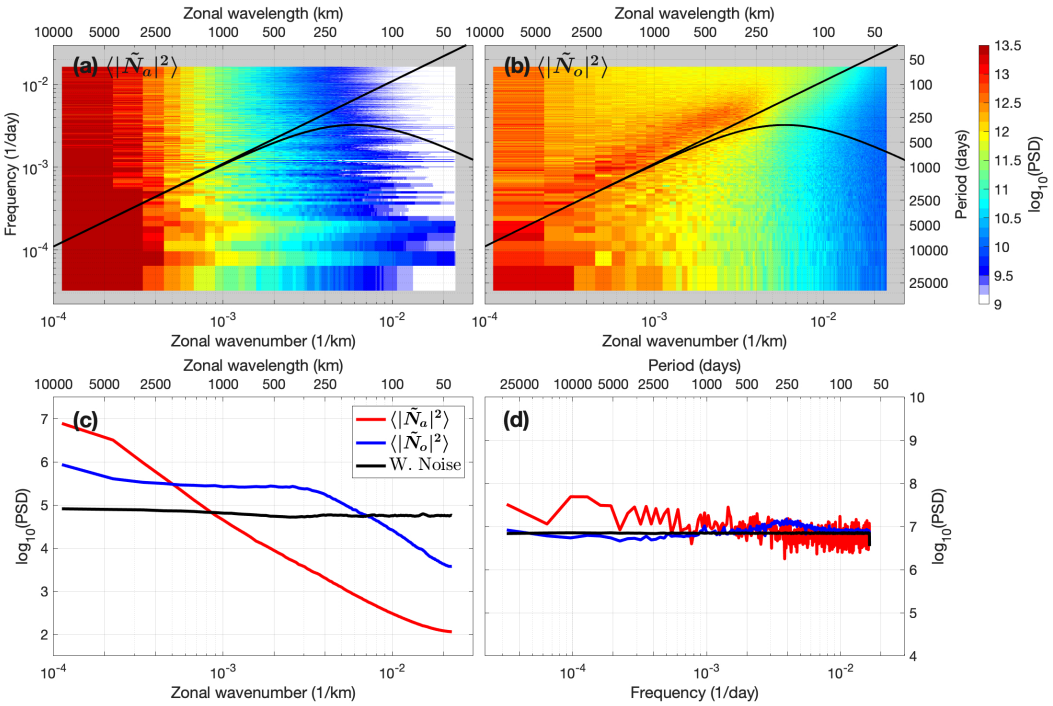

Figure 2. Top (a-b): $\langle|\tilde{N}_o|^2\rangle$ and $\langle|\tilde{N}_a|^2\rangle$ power spectral densitites (PSD) computed as a function of zonal wavenumber (k) and frequency (ω) using HR data at 40°S in the Pacific Ocean. The overlaid curved line represent the dispersion relation for first mode baroclinic oceanic Rossby waves, while the straight line shows the non-dispersive wave limit. Bottom (c-d): $\langle|\tilde{N}_o|^2\rangle$ and $\langle|\tilde{N}_a|^2\rangle$ integrated over one dimension to highlight their variation as a function of either k or ω (red and blue lines, respectively). The black lines are correspondent estimates computed using white noise.

3.1 Geophysical noise vs. white noise forcing spectra

Estimates of $\langle|\tilde{N}_o|^2\rangle$ and $\langle|\tilde{N}_a|^2\rangle$ defined using geophysical noise and white noise are shown Fig. 2. These are computed for σ_o^2 and σ_a^2 equal to one in order to highlight differences between the shape of the oceanic and atmospheric geophysical noise power spectra when compared to white spectra.

The geophysical $\langle|\tilde{N}_a|^2\rangle$ includes slightly larger variances toward lower frequencies than the correspondent white noise estimate – thus, it is slightly more red (Fig. 2d). It is also prominently red in zonal wavenumber domain, with the power decaying toward higher wavenumbers at an approximate k^{-3} rate over scales ∼1000-4000 km and at a slower k^{-2} rate over scales smaller than 1000 km (Fig. 2c). This distribution resembles that estimated for tropospheric winds using aircraft measurements (Nastrom & Gage,

1985; Cho et al., 1999; Tulloch & Smith, 2009; Callies et al., 2014), although the latter was found to decay at a $k^{-5/3}$ rate over scales smaller than 1000 km.

In turn, the geophysical $\langle|\tilde{N}_o|^2\rangle$ is white in frequency space (Fig. 2d). In zonal wavenumber domain, it has a plateau between ∼300-6000 km and a k^{-2} slope at smaller spatial scales (Fig. 2c). The spectrum computed as a function of both k and ω (Fig. 2b) show that the variances are larger near the dispersion relation for first mode baroclinic Rossby waves and its non-dispersive limit, here computed using an observational climatology of the first internal Rossby radius of deformation (Chelton et al., 1998). This correspondence was also previously reported in satellite-based estimates of SST, sea surface height, ocean color (Early et al., 2011; Chelton, Schlax, & Samelson, 2011; Chelton, Gaube, et al., 2011; O'Brien et al., 2013), and in positively-correlated SST and 10-m wind signals (Laurindo et al., 2019). This characteristic can reflect variability induced by linear Rossby waves and by nonlinear mesoscale ocean phenomena such as coherent eddies and zonal jets (Early et al., 2011; Chelton, Gaube, et al., 2011; Berloff & Kamenkovich, 2013a, 2013b; Polito & Sato, 2015). Here, it is observed over much of the extratropics except at the latitudes of strong current systems such as the ACC and the Kuroshio Current, potentially owing to the influence of strong currents on the dispersion characteristics (Laurindo et al., 2019). Corresponding $\langle|\tilde{N}_o|^2\rangle$ and $\langle|\tilde{N}_a|^2\rangle$ estimates for LR (not shown) reveal characteristics similar to those described for HR, except that $\langle|\tilde{N}_o|^2\rangle$ decay at an $\sim k^{-1}$ rate over zonal wavelengths between ∼600-6000 km.

3.2 Spectra predicted by the stochastic model solutions

Stochastic model estimates of the SST power spectra (G_{TT}), and of the THF power spectra (G_{QQ}) for $\langle|\tilde{N}_o|^2\rangle$ (ocean-driven, OCN) or $\langle|\tilde{N}_a|^2\rangle$ (atmosphere-driven, ATM) forcing are illustrated in Fig. 3, contrasting results obtained using geophysical and white noise forcing. Here, the forcing spectra also integrate to variances equal to one with the goal of illustrating the shape of the G_{TT} and G_{QQ} response spectra rather than show estimates with realistic magnitudes.

The stochastic model solutions do not depend on k by construction [Eqs. (7)-(9)], such that variations in zonal wavenumber domain must originate in $\langle|\tilde{N}_o|^2\rangle$ and $\langle|\tilde{N}_a|^2\rangle$. Thus, the OCN and ATM components of G_{TT} and G_{QQ} computed using white noise are also white in k, while estimates obtained using geophysical noise mirror the shape of the forcing spectra (Fig. 3, left panels).

In turn, G_{TT} and G_{QQ} estimates computed as a function of ω (Fig. 3, right panels) indicate that both types of noise forcing give rise to similar results, although ATM

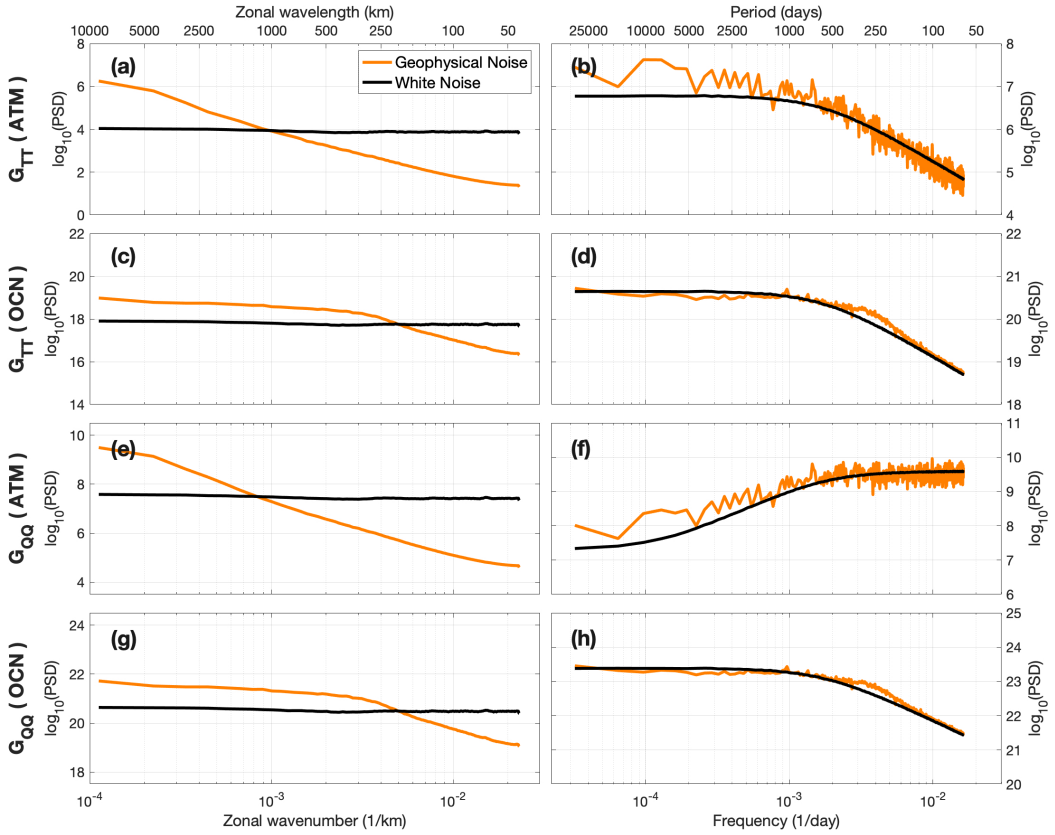

Figure 3. Estimates of atmosphere-driven (ATM) and ocean-driven (OCN) components of the G_{TT} and G_{QQ} power spectral densities (PSD) computed as a function of zonal wavenumber (k, left panels) and frequency (ω, right) using $\langle|\tilde{N}_o|^2\rangle$ and $\langle|\tilde{N}_a|^2\rangle$ forcing spectra defined using white noise (black lines) and HR data referent to 40°S in the Pacific Ocean (geophysical noise, orange lines).

estimates computed using geophysical noise show more power at low frequencies than estimates obtained with white noise (Figs. 3b and 3f) because the former is slightly redder in frequency space to begin with (c.f. Fig. 2d). Starting with the ATM component of G_{TT} (Fig. 3b), the spectrum is prominently red and shows a plateau over periods between ∼1000 days and 80 years, whose power decays at an approximate $\omega^{-5/3}$ rate toward higher frequencies. To understand how the stochastic forcing drives a red spectrum SST response in frequency domain, attention is called to the denominator of the analytical solution of G_{TT} [Eq. (7)]. At high frequencies, $4\pi^2\omega^2 \gg (\alpha+\beta)^2$ and the spectrum varies as an inverse function of ω^2, thus increasing toward longer periods. In contrast, $4\pi^2\omega^2 \ll (\alpha+\beta)^2$ at low frequencies thereby scaling solely as a function of $1/(\alpha+\beta)^2$. These characteristics were widely used in the past to explain the low-frequency SST variability emerging in response to stochastic atmospheric forcing at oceanic regions away from strong current systems (e.g., Hasselmann, 1976; Frankignoul & Hasselmann, 1977; Barsugli & Battisti, 1998; Frankignoul et al., 1998; von Storch, 2000). Here, the stochastic model solutions predict a similar red spectrum structure for the OCN component of G_{TT}, suggesting that stochastic forcing by ocean processes can also give rise to low-frequency variability in SST.

The ATM component of G_{QQ} shows more power over higher frequencies (a "blue" spectrum) (Fig. 3f). The analytical solution [Eq. (8)] indicates that the blue spectrum response arises from the presence of $4\pi^2\omega^2+\beta^2$ on the numerator and of $4\pi^2\omega^2+\alpha+\beta)^2$ in the denominator. Over periods shorter than ∼1000 days, the dependence on ω^2 in both the numerator and denominator approximately cancel each other, resulting in a white power spectrum. Toward lower frequencies, however, the absence of α in the numerator implies a larger relative importance of ω^2 relative to the damping terms than in the denominator, causing the total power to diminish for increasing periods. In turn, the OCN component of G_{QQ} (Fig. 3h) show a red spectrum structure similar to that of G_{TT}, indicating that the low-frequency SST variability induced by ocean processes are mirrored in THF.

The stochastic model estimates of the cross-spectral statistics coherence (γ^2_{TQ}) and absolute phase factor ($|\theta_{TQ}|$) are sensitive to the relative strength of the ocean and atmosphere forcing (Fig. 4), reason for which they are analysed as a function of the ratio between the integrated variances of $\langle|\tilde{N}_o|^2\rangle$ and $\langle|\tilde{N}_a|^2\rangle$ (σ^2_o and σ^2_a, respectively). Here, the ratio is normalized by λ^2_q so that values equal to one indicate that the oceanic and atmospheric forcing contribute equally to the integrated SST variance.

Estimates of γ^2_{TQ} and $|\theta_{TQ}|$ reveal distinct linear spectral relationships when either the atmosphere or ocean forcing are strong (Fig. 4). When the atmosphere forc-

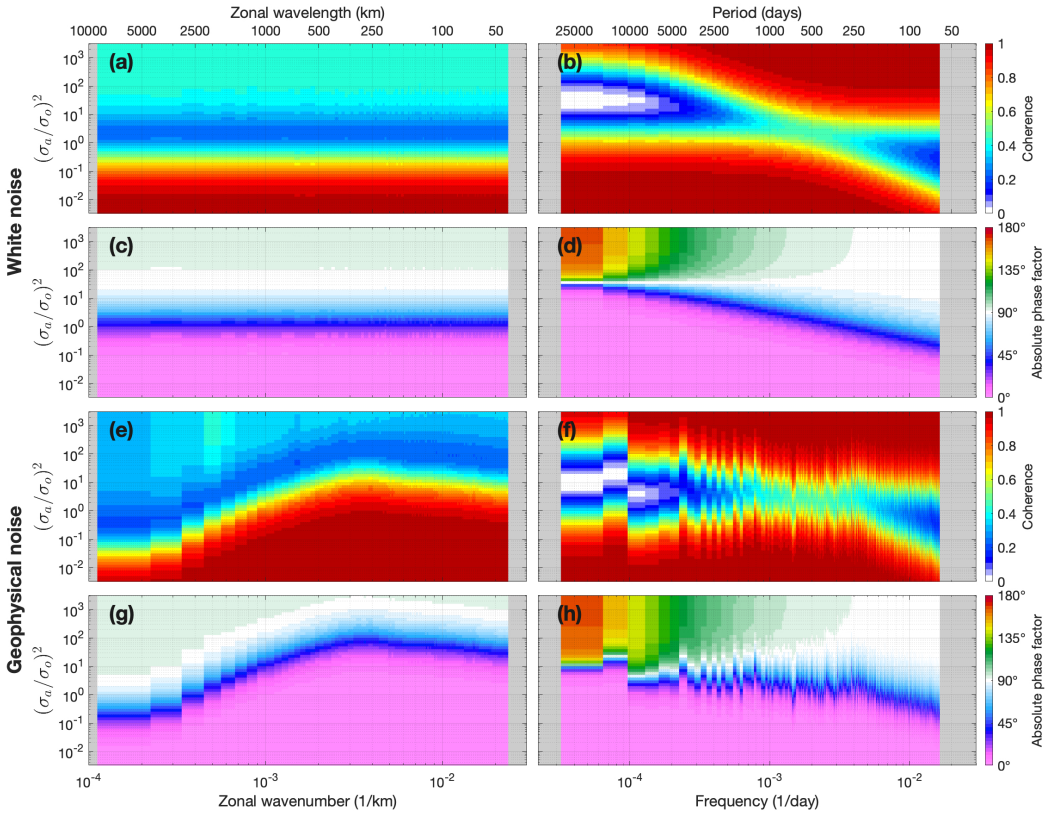

Figure 4. Stochastic model estimates of the coherence (γ^2_{TQ}) and absolute phase factor ($|\theta_{TQ}|$) between upper-50 m ocean temperature and THF as a function of zonal wavenumber (k, left column) and frequency (ω, right column). The results are computed using $\langle|\tilde{N}_o|^2\rangle$ and $\langle|\tilde{N}_a|^2\rangle$ defined using white noise (panels a-d) and using HR data for 40°S in the Pacific (geophysical noise, panels e-h), and vary as a function of the ratio between the integrated variances of the forcing spectra $[(\sigma_a/\sigma_o)^2]$.

ing is dominant, estimates in k domain show ∼0.4 coherences associated with 90° phase factors, while estimates computed in as a function of ω show coherences equal to one and phases varying from 90° at periods shorter than ∼1000 days to 180° at periods close to 80 years. The smaller coherences in k results from weak relationships between SST and THF at zero temporal lag. In turn, the coherences approaches one while associated with a 0° phase in both k and ω domains when the ocean forcing is dominant.

γ^2_{TQ} and $|\theta_{TQ}|$ shows no dependence in k when computed using white noise, varying solely as a function of $(\sigma_a/\sigma_o)^2$ (Figs. 4a and 4c). In contrast, estimates obtained using geophysical noise (Figs. 4e and 4g) reveal a clear dependence on k, with γ^2_{TQ} and $|\theta_{TQ}|$ values characteristic of atmosphere-driven variability transitioning to ocean-driven at wavelengths varying from ∼2500 to 300 km for $(\sigma_a/\sigma_o)^2$ increasing from $\sim 10^{-1}$ to 10^1. This indicates that stronger ocean forcing leads to transitions from ocean to atmosphere-driven variability at longer wavelengths. In the frequency domain, γ^2_{TQ} and $|\theta_{TQ}|$ estimates for white and geophysical noise both show that ocean forcing can influence the cross-spectral statistics more efficiently at low-frequencies than at high-frequencies (Fig. 4, right column). This feature arises as a consequence of the low-frequency response in both SST and THF induced by ocean forcing while the atmosphere modulates THF at high frequencies (c.f. Fig. 3).

In summary, this Section demonstrates that using $\langle|\tilde{N}_o|^2\rangle$ and $\langle|\tilde{N}_a|^2\rangle$ defined with geophysical noise rather than white noise in the FCL98 stochastic model solutions give rise, in the zonal wavenumber domain, to variance distributions in the OCN and ATM components of G_{TT} and G_{QQ} that mirror that of the forcing spectra. The use of geophysical noise also introduce a spatial-scale dependence in γ^2_{TQ} and $|\theta_{TQ}|$ that is absent in estimates obtained using white noise. In the frequency domain, the results are similar for both types of forcing signals and show that, while stochastic atmosphere forcing produces a red spectrum response in G_{TT}, it induces a blue spectrum response in G_{QQ}. In contrast, ocean forcing induces a red spectrum response in both G_{TT} and G_{QQ}, suggesting that ocean processes are more effective in determining γ^2_{TQ} and $|\theta_{TQ}|$ at low frequencies than the atmosphere.

4 Results

4.1 SST and THF variances from observations, HR, and LR

To provide a background to the analysis of the spectral quantities computed using HR, LR, and OBS data, this Section briefly describes the horizontal distributions of the monthly SST and THF variances for each of the datasets.

The SST variance from OBS is larger in strong current systems and in the tropics (Fig. 1a). More specifically, the largest values (> 1.0 K^2) coincide with western boundary currents and their seaward extensions, the equatorial current system in the Pacific, the ACC, the Brazil-Malvinas Confluence, and the Agulhas Retroflection. Within the Tropical Pacific, high variances are associated with El Niño-Southern Oscillation (ENSO) events and with zonally-progapating intraseasonal Rossby waves and Tropical Instability Waves (TIWs), while at the extratropical current systems it is predominantly driven by mesoscale ocean phenomena such as coherent eddies and meanders. Away from these energetic systems, variances of O(0.1-1.0 K^2) are found within the subtropical gyres of all major ocean basins. Over monthly timescales, the SST variability in these regions is predominantly driven by the atmosphere via turbulent heat fluxes (Bishop et al., 2017; Small et al., 2019), although it also includes the signature of westward-propagating ocean eddies (Chelton, Schlax, & Samelson, 2011; Laurindo et al., 2019). The THF variance from OBS (Fig. 1b) noticeably lacks the enhanced variances at the tropical Pacific found in the SST estimates, but similar spatial features (as in SSTs) are found in the extratropics. THF variances of $\sim$1000-5000 (W/m^2)^2 are seen in the Labrador Sea and at strong current systems, most prominently the Gulf Stream and the Kuroshio Currents, while the interior of the subtropical gyres show values between $\sim$500-1500 (W/m^2)^2.

The SST and THF variance distributions in HR are similar to that of OBS, although ratios between the datasets indicate that the HR values can be two to ten times larger than OBS within the extratropical current systems (Figs. 1c-d). In contrast, the lack of resolved mesoscale phenomena in LR leads to the underestimation of the SST and THF variances relative to HR and OBS over much of the extratropics, specifically by factors of $\sim$10 in the eddy-rich regions and of $\sim$2 within the subtropical gyres (Figs. 1e-h). Previous assessments showed that the higher SST variability in HR relative to LR is caused by the larger upper-ocean heat flux convergence by the resolved mesocale ocean variability, which induces a corresponding increase on the THF variability (Kirtman et al., 2012; Putrasahan et al., 2017; Small et al., 2019, 2020). The results of the spectral analysis, described next, determines the spatial and temporal scales where resolved ocean phenomena induce such a response in both quantities.

4.2 Power spectra and cross-spectral statistics

4.2.1 Zonal wavenumber spectra:

The zonal wavenumber SST power spectra (G_{TT}) from all datasets (HR, LR and OBS) show similar magnitudes at zonal wavelengths between $\sim$2500-7000 km and vary as k^{-3} as also seen at 40°S (Fig. 5a). Toward smaller scales, HR and OBS estimates no-

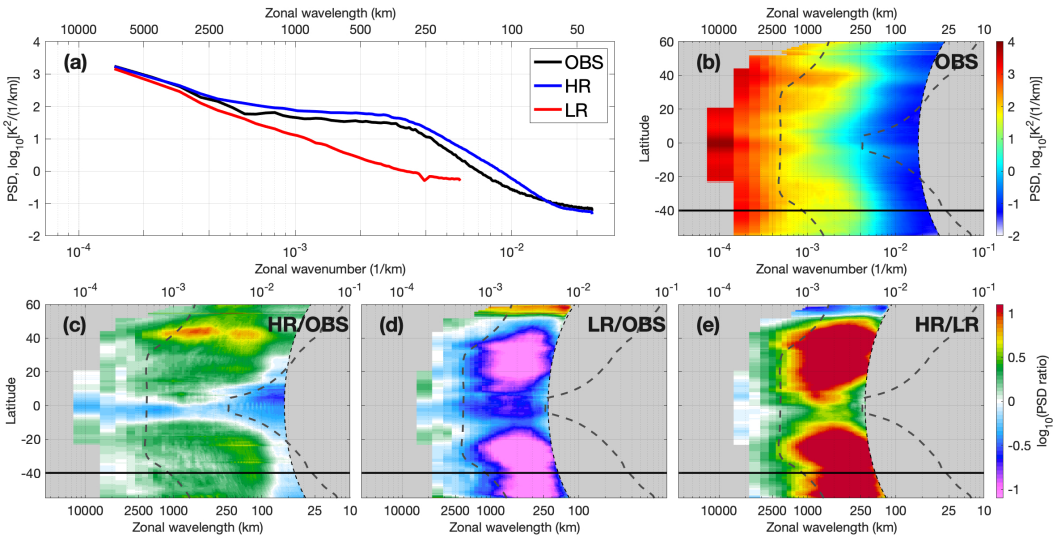

Figure 5. Power spectral density (PSD) of SST (G_{TT}) computed as a function of zonal wavenumber (k) for the Pacific Ocean using HR, LR, and OBS data. Panel (a) show the power spectra retrieved for 40°S, (b) is the latitudinal spectrogram for OBS, (c-d) show the ratio of the OBS estimates relative to the HR and LR results, and (e) the ratio between the HR and LR results. The left and right thick dashed lines in (b-e) represent the zonally-averaged first internal Rossby radius of deformation for the ocean and the atmosphere, respectively, the thin dashed line marks the spatial Nyquist frequency for the spectral analysis, and the black horizontal line denotes the 40°S latitude used to plot the results shown in (a).

ticeably diverge from LR, showing a plateau between ∼300-2000 km and then decaying at a $\sim k^{-4}$ rate between ∼70-300 km, while the LR estimates maintain the steep k^{-3} decay rate until ∼300 km zonal wavelengths. These distinct shapes result in a much larger SST variance in HR and OBS relative to LR over scales smaller than about 2000 km. Similar results are found for the THF power spectra (G_{QQ}) (not shown).

The spectrograms of G_{TT} as a function of latitude (Figs. 5b-e) indicate that the spectral characteristics observed at 40°S occur over much of the extratropics. The same is observed in corresponding G_{QQ} estimates (not shown). To support the interpretation of the spectrograms, they are overlaid by the meridional profile of the zonally-averaged first internal Rossby radius of deformation (R_1) for the atmosphere and the ocean. Here, the atmospheric R_1 is computed using time-averaged potential temperature data for the troposphere obtained from the National Centers for Environmental Prediction (NCEP)

reanalysis model (Kalnay et al., 1996), while the oceanic R_1 is taken from the Chelton et al. (1998) observational climatology.

The ratio between the power spectra resolved by each dataset indicate that the largest differences between HR and OBS relative to LR (factors of ten or more) usually occurs at wavelengths smaller than the atmospheric R_1, which increases from ∼600 km at 60° latitude in both hemispheres to ∼2000 km within the tropics. Despite the SST and THF spectra resolved by HR are closer in magnitude and overall shape to OBS than LR, in the extratropics they exceed the magnitude of OBS at most wavenumbers, most prominently at the latitudes of strong current systems, such as between 35-50°N where the seaward extensions of the Kuroshio and Oyashio Currents occur (Fig. 5c). The ratio between the SST (THF) variances resolved by HR and OBS, averaged over all latitudes and wavenumbers, is 1.60 (1.13). For 35-50°N, this value increases to 2.69 (2.16).

The coherence (γ^2_{TQ}) for all of the datasets is low (∼0.2) and the phase ($|\theta_{TQ}|$) is ∼90° at wavelengths larger than approximately 2000 km (Fig. 6). A detailed examination at 40°S (Figs. 6a-b) shows that, towards smaller scales, γ^2_{TQ} increases in HR and OBS reaching ∼0.9 between 250-500 km, while $|\theta_{TQ}|$ approaches zero. At scales smaller than 250 km, the coherence in OBS steadily decrease until ∼0.2 at about 100 km. The coherence is larger in HR than in OBS over most spatial scales, maintaining values above 0.7 at 100 km, which then sharply decreases to ∼0.2 near the limit of the analysis at approximately 50 km. In contrast, at 40°S LR shows a coherence of about 0.2 throughout the analyzed wavenumber range, with minimum phase factors of about 50° between ∼700-2500 km that return to 90° toward smaller scales.

The latitudinal spectrograms of γ^2_{TQ} and $|\theta_{TQ}|$ (Figs. 6c-h) indicate that OBS and HR resolves the band of high coherences associated with near-zero phase factors at most latitudes, with the largest γ^2_{TQ} values (> 0.5) observed in the extratropics and over spatial scales smaller than the atmospheric R_1. Interestingly, the LR results also show smaller phase factors at smaller spatial scales in the extratropics, with $|\theta_{TQ}|$ approaching zero at the the latitudes of the Kuroshio and Oyashio Currents (∼35°-50°N) and within the tropics, both features associated with coherences of about 0.4.

To enable a physical interpretation of the spectra computed using OBS, HR, and LR data, Figs. 7 and 8 show corresponding estimates obtained using the FCL98 stochastic model. These are best-fit estimates computed using the methods described in Sec. 2.3 and Appendix A, and are distinguished from the spectra obtained using SST and THF data (hereafter referred to as reference results) by variables adorned by primes (hence G'_{TT}, G'_{QQ}, $\gamma^{2'}_{TQ}$, and $|\theta'_{TQ}|$). Here, OCN denotes stochastic model estimates computed

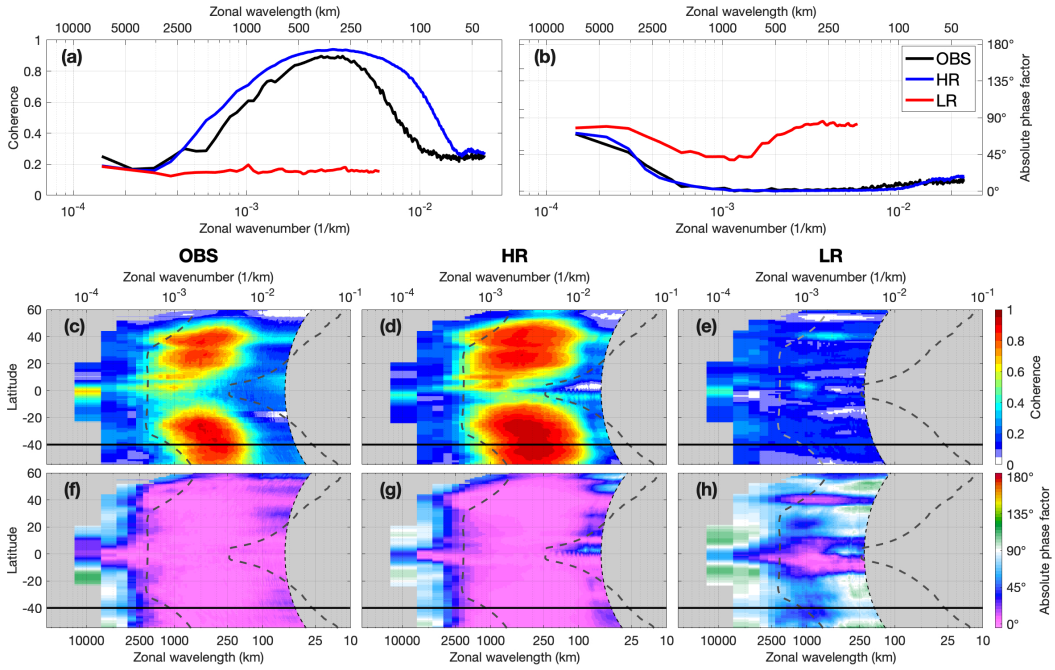

Figure 6. Coherence (γ^2_{TQ}) and absolute phase factor (θ_{TQ}) between SST and THF in zonal wavenumber domain (k) for the Pacific Ocean resolved by HR, LR, and OBS. The top row (a-b) exemplify estimates for 40°S while the middle (c-e) and bottom (f-h) rows show latitudinal spectrograms. The left and right thick dashed lines in (c-h) represent the zonally-averaged first internal Rossby radius of deformation for the ocean and the atmosphere, respectively, the thin black dashed denotes the spatial Nyquist frequency for the spectral analysis, while the black horizontal line marks the 40°S latitude that the estimates in panels (a-b) refer to.

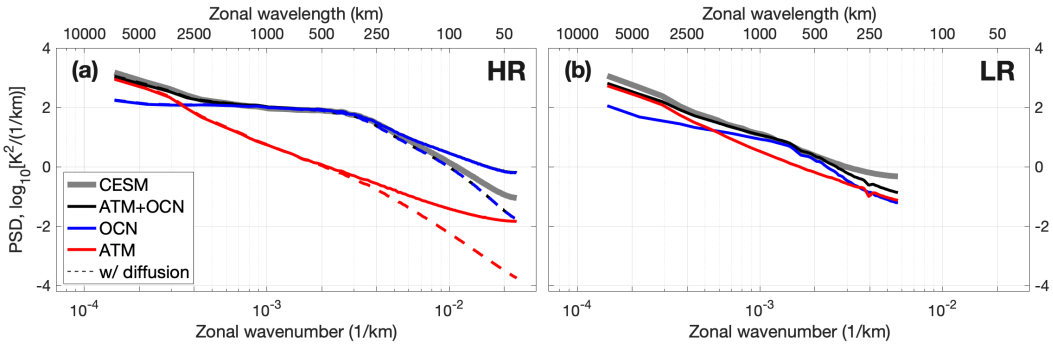

Figure 7. Best-fit stochastic model estimates of the zonal wavenumber (k) power spectral density (PSD) of SST (G'_{TT}) for HR and LR (panels a and b, respectively) for 40°S in the Pacific Ocean. The panels show the ocean-driven (OCN) and atmosphere-driven (ATM) components of the stochastic model solutions (blue and red lines, respectively), and of their sum (ATM+OCN, black). The continuous lines are results obtained using the stochastic model formulation proposed in Sec. 2.3, while the dashed lines denote estimates denote estimates obtained using a formulation extended to include a diffusion term, assuiming an eddy diffusivity coefficient equal to 100 m^2/s. The thick gray lines are the reference SST spectra computed using CESM data.

using solely the $\langle|\tilde{N}_o|^2\rangle$ forcing spectra (where $\langle|\tilde{N}_a|^2\rangle = 0$), while ATM denotes estimates obtained using $\langle|\tilde{N}_a|^2\rangle$ ($\langle|\tilde{N}_o|^2\rangle = 0$).

The G'_{TT} estimate for HR at 40°S (Fig. 7a) indicates that ATM has larger magnitudes than OCN at zonal wavelengths longer than ∼2500 km. Toward smaller scales, the variance in ATM decreases steeply at an approximate k^{-3} rate and is then surpassed by OCN, which accounts for the plateau observed between ∼300-2000 km – hence implying that this feature arises from the action of ocean processes. Corresponding results for LR (Fig. 7b) show that the ATM component is similar in shape and magnitude to that obtained for HR, however significantly smaller variances in OCN, resulting in a total G'_{TT} spectrum with shape similar to that of ATM. Estimates of G'_{QQ} for both HR and LR (not shown) reveal characteristics similar to those described for G'_{TT}.

At wavelengths smaller than ∼300 km, G'_{TT} (Fig. 7a) and G'_{QQ} (not shown) estimates for HR are found to decay at a slower k^{-4} rate than the k^{-2} found in reference HR results. However, the stochastic model solutions can reproduce the approximate k^{-4} slope if a diffusion term $[\kappa(\partial^2 T/\partial x^2)]$ is added to Eq. (5) with an eddy diffusivity coefficient $\kappa = 100$ m^2/s, defined empirically. The impact of including a diffusion term in

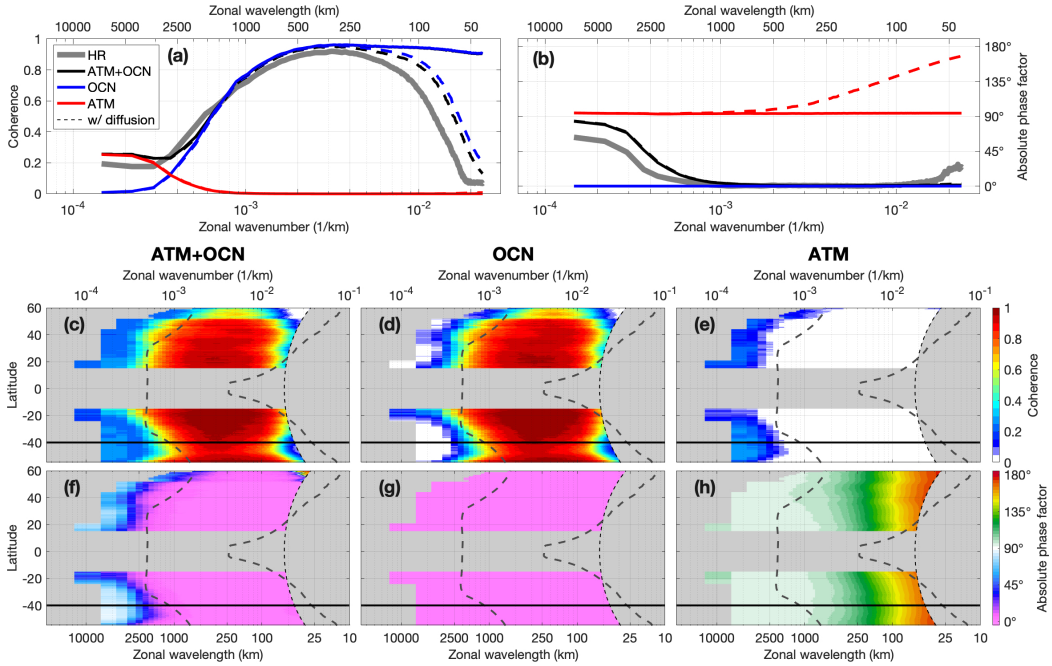

Figure 8. Best-fit stochastic model estimates of the coherence ($\gamma^{2'}_{TQ}$) and absolute phase factor ($|\theta'_{TQ}|$) between SST and THF as a function of zonal wavenumber (k) for HR. The top row (a-b) exemplifies the ocean and atmosphere-driven components of the stochastic model solutions (OCN and ATM, blue and red lines, respectively), their sum (ATM+OCN, black), and the reference estimates from the HR simulations (thick gray line). The middle (c-e) and bottom (f-h) rows are latitudinal spectrograms of the ATM+OCN, OCN, and ATM components of $\gamma^{2'}_{TQ}$ and $|\theta'_{TQ}|$, respectively. The left and right dashed lines in (c-h) represent the zonally-averaged first internal Rossby radius of deformation for the ocean and the atmosphere, respectively, the thin dashed line is the spatial Nyquist frequency for the spectral analysis, and the black horizontal line marks the 40°S latitude used to plot the results in (a-b).

corresponding LR estimates was negligible. The justification for adding the diffusion term to the FCL98 stochastic model is further discussed in Sec. 5.3.

Further, $\gamma^{2'}_{TQ}$ and $|\theta'_{TQ}|$ estimates reproduce spectral characteristics seem in the reference HR results (Fig. 8) and LR results (not shown). For HR, they demonstrate that the low coherence/90° phase relationship at spatial scales larger than the atmospheric R_1 in the extratropics reflects variability in SST and THF driven by atmospheric processes. In addition, the high coherence and near-zero phase at smaller scales reflects variability predominantly driven by ocean processes (Figs. 8c-h). Moreover, Figs. 8a-b contrasts best-fit estimates including and not including diffusion effects, and indicate that neglecting the diffusion leads to coherences that remain high (∼0.9) at zonal wavelengths smaller than about 300 km rather than decaying to ∼0.2 values as shown by the reference results. Interestingly, the diffusion term introduces a dependence on k in the ATM component of $|\theta'_{TQ}|$. Here, the phase gradually increase from 90° at about 1000 km to 180° near the limit of the analysis at ∼50 km. It is noted that the latitudinal spectrograms in Figs. 8c-h are stochastic model solutions that include the diffusion effect.

Finally, corresponding $\gamma^{2'}_{TQ}$ and $|\theta'_{TQ}|$ estimates for LR (not shown) indicate that the smaller variance in OCN significantly reduces the coherence at spatial scales smaller than the atmospheric R_1 and tend to produce larger values of $|\theta'_{TQ}|$ relative to the reference HR estimates (Fig. 8). Although the imprint of ocean processes in the best-fit cross-spectral statistics are stronger than implied by the reference LR estimates (Figs. 6e and 6h), these results suggest that the reduction in the phase factors from 90° to ∼50° over scales smaller then the atmospheric R_1 associated with the slightly enhanced coherences of ∼0.4 near the equator and at the latitude of the Kuroshio and Oyashio Currents reflect a response of the air-sea coupling characteristics to the ocean dynamics resolved in LR, albeit one that is much weaker than that present in HR and OBS.

To summarize, this Section demonstrates that HR resolves a more realistic SST and THF power spectra and cross-spectral statistics in the zonal wavenumber domain than LR at most latitudes. It also shows that, in the extratropics, corresponding stochastic model estimates can reproduce key spectral features in both simulations, suggesting that the stochastic model is a valid physical model for interpreting the roles of oceanic and atmospheric processes in their control of the spectra. In particular, these results show that the atmosphere dominates the SST and THF variability over zonal wavelengths larger than about 2000-2500 km. Toward smaller wavelengths, HR and OBS estimates suggest resolved mesoscale ocean processes explain most of the SST and THF variability and covariability over wavelengths between 100 km and the atmospheric R_1 (∼600-2000 km), scales that are thus longer than the typical mesoscale range [$\mathcal{O}(10^1$-10^2 km)]. Diffusion

583 effects also become important at scales of ∼300 km or less. The significant influence of
584 ocean processes is seen not only at the latitudes of intense, nearly zonal extratropical
585 current systems (such as the Kuroshio and Oyashio Currents) but also at more quies-
586 cent regions such as the subtropical gyres.

587 ***4.2.2 Frequency spectra:***

588 This Section now examines spectral quantities computed in frequency domain for
589 the Pacific Ocean. First considering G_{TT} estimates for OBS, HR, and LR, the spectra
590 from all datasets is red throughout the analyzed latitudes (Figs. 9a-b). In the extrat-
591 ropics, the ratio between estimates from each dataset (Figs. 9c-e) indicate that OBS and
592 HR resolve variances larger than LR at most frequencies, with the largest differences at
593 periods shorter than about 1000 days. In contrast, G_{QQ} is approximately white in LR
594 for all for frequencies (Fig. 9f). Corresponding OBS and HR estimates show G_{QQ} vari-
595 ance levels similar to LR at intraseasonal timescales, which increase significantly rela-
596 tive to LR over intraseasonal to annual periods. At periods longer than annual, the G_{QQ}
597 for HR and OBS then becomes approximately white (Figs. 9f-j).

598 To interpret the differences of G_{TT} and G_{QQ} resolved by LR relative to those in
599 HR and OBS, focus is given on 40°S as representative of their behaviour in the extra-
600 tropics (left panels in Fig. 10). The contrast between the reference estimates with cor-
601 responding best-fit stochastic model results (G'_{TT} and G'_{QQ}) suggest that the larger SST
602 and THF variances in HR relative to LR likely arises from the action of ocean processes,
603 since best-fit estimates of the atmosphere-driven component (ATM) for both HR and
604 LR show similar shape and magnitudes while the ocean-driven component (OCN) are
605 significantly larger in HR.

606 The stochastic model solutions predict that both oceanic and atmospheric processes
607 both produce a red spectrum response in G'_{TT} (Figs. 10a and 10c), although its ATM
608 component is redder than OCN because the forcing spectrum defined for the atmosphere
609 is slightly red while for the ocean it is nearly white (c.f. Sec. 3.2, Figs. 3, 4b, and 4d).
610 In HR, this leads to ATM with magnitudes generally larger than OCN at periods longer
611 than about 1000 days, and to larger variances in OCN over higher frequencies. In LR,
612 OCN is weaker than ATM throughout.

613 In contrast, G'_{QQ} estimates for HR (Figs. 10e and 10g) indicate that ATM accounts
614 for most of the turbulent heat flux variability at periods shorter than 500 days while OCN
615 is dominant at longer periods. In LR, even though the ocean-driven component is much
616 smaller than in HR, it also explains most of the THF variability over periods longer than

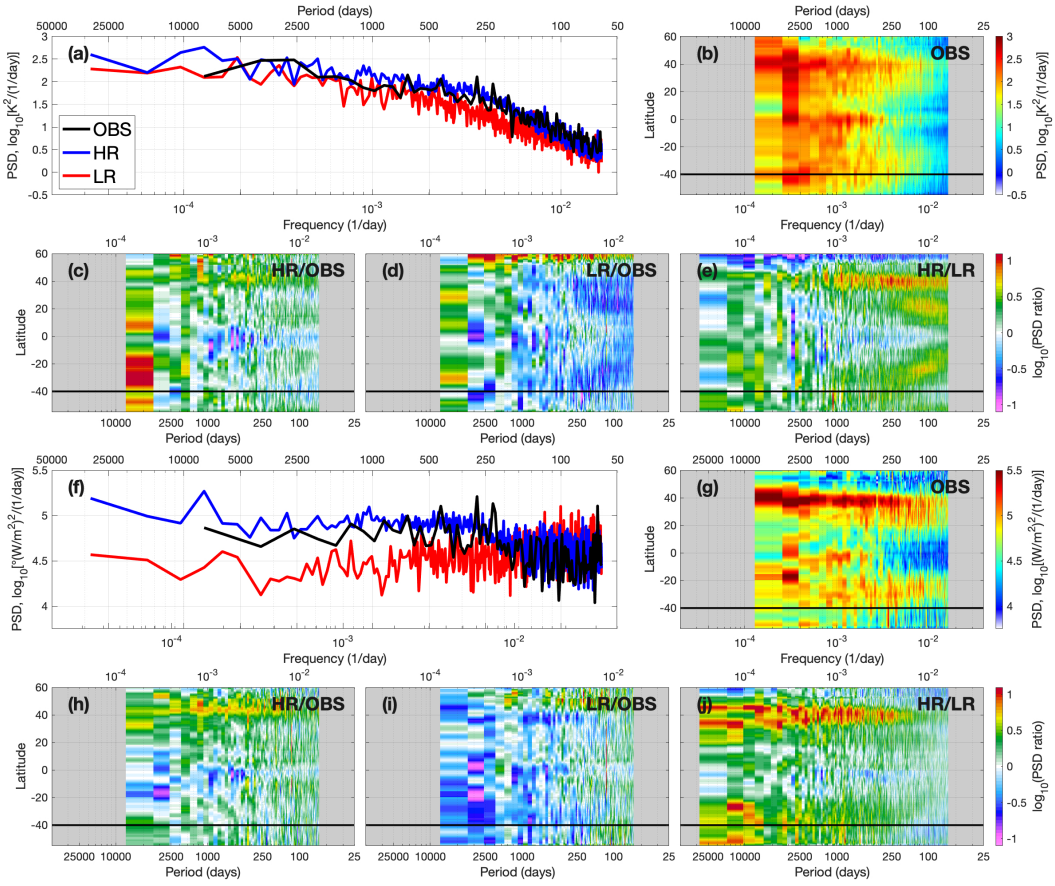

Figure 9. Power spectral density (PSD) of SST (G_{TT}) and THF (G_{QQ}) computed as a function of frequency (ω) for the Pacific Ocean using HR, LR, and OBS data. Panel (a) show G_{TT} estimates retrieved for 40°S, (b) is the latitudinal G_{TT} spectrogram for OBS, (c-d) show the ratio of the OBS estimates shown in (b) relative to the HR and LR results, and (e) the ratio between the HR and LR results. Panels (f-g) show corresponding results for G_{QQ}. The black horizontal line denotes the 40°S latitude used to plot the results in panels (a) and (f).

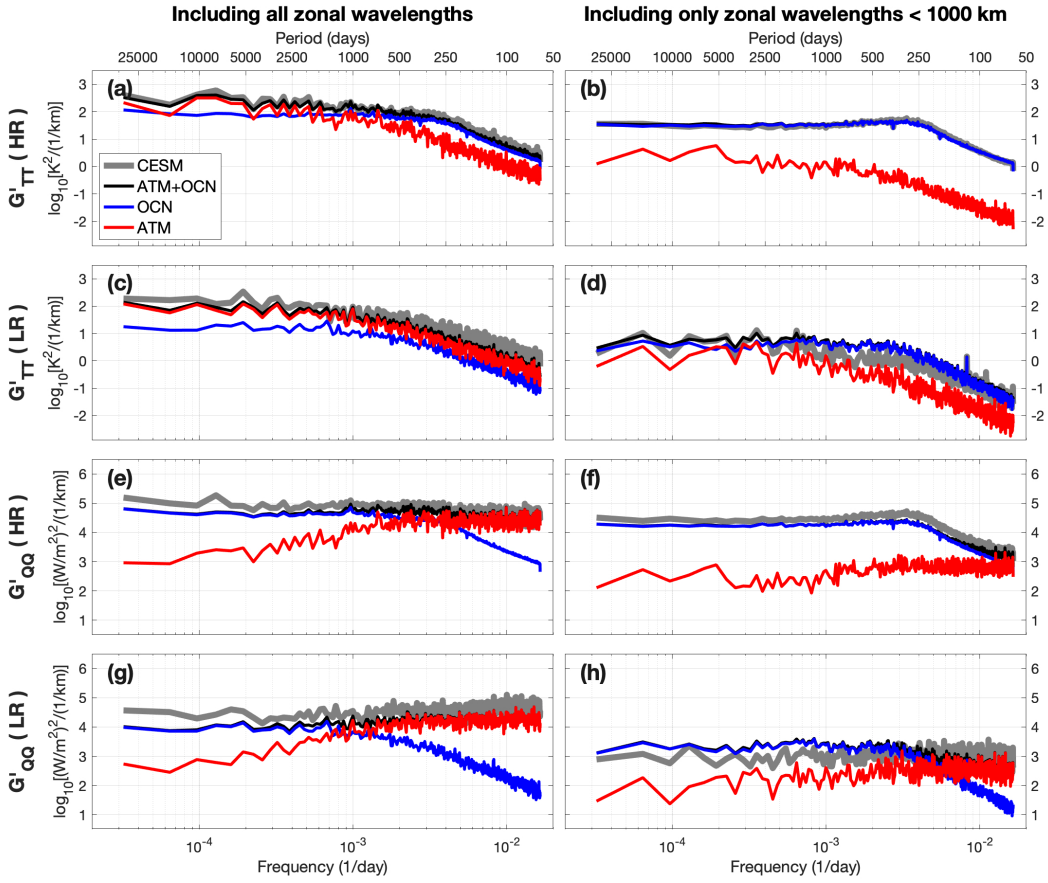

Figure 10. Best-fit stochastic model estimates of the frequency (ω) power spectrum of SST (G'_{TT}, panels a-d) and THF (G'_{QQ}, e-h) for HR and LR, illustrated for 40°S in the Pacific Ocean. The left column show estimates integrated over all zonal wavelengths, while the results in the right column are integrated over wavelengths smaller than 1000 km. In all panels, the blue and red lines refers to the ocean and atmosphere-driven components of the stochastic model solutions (OCN and ATM, respectively), and the black lines shows their sum (ATM+OCN). The thick gray lines show the reference SST and THF spectra from HR and LR.

about 1000 days. These characteristics are explained by the fact that, while ocean forcing produces a red spectrum response in the turbulent heat fluxes, the atmospheric forcing drives a blue response spectrum where the variances decrease toward lower frequencies (c.f. Sec. 3.2, Figs. 4f and 4h).

To further evaluate the importance of resolved ocean processes in the SST and THF variability, the right panels in Fig. 10 show frequency-domain G_{TT} and G_{QQ} (and corresponding best-fit stochastic model G'_{TT} and G'_{QQ}) estimates for HR and LR computed for zonal wavelengths smaller than 1000 km, thus isolating scales that the zonal wavenumber analysis (Sec. 4.2.1) suggests to be dominated by ocean processes. For HR, filtering out the large scales produce reference G_{TT} and G_{QQ} spectra (Figs. 10b and 10f) that are both red and similar to OBS (not shown), with corresponding best-fit estimates indicating that OCN accounts for most of the variance of both quantities. LR estimates show significantly smaller variances in G_{TT} and G_{QQ} relative to HR and OBS, attributed by the best-fit results to a small ocean-driven variability (Figs. 10d and 10h).

Estimates of the cross-spectral statistics γ^2_{TQ} and $|\theta_{TQ}|$ computed for OBS and HR considering zonal wavelengths smaller than 1000 km (Fig. 11) reveal near-zero phase factors at all latitudes and over the entire frequency range, with the highest coherences (>0.4) occurring in the extratropics. The γ^2_{TQ} for OBS and HR also indicate that enhanced values usually appear over higher frequencies toward the equator, characteristic compatible with oceanic Rossby waves and coherent eddies (Laurindo et al., 2019), and tend to persist until the lowest frequencies resolved by the analysis (Figs. 11c-d). In LR, the γ^2_{TQ} and $|\theta_{TQ}|$ estimates show sharp variations in frequency domain at most latitudes, although a tendency for near-zero phases can be observed near the equator and at 40°N at most frequencies (Fig. 11h). In addition, near-zero phase is also seen at most latitudes over periods longer than about 2500 days.

Best-fit estimates of the coherence and absolute phase factor ($\gamma^{2'}_{TQ}$ and $|\theta'_{TQ}|$, respectively) for HR (Fig. 12) are visually similar to the OBS and HR results in Fig. 11. Thus, in the extratropics, ocean forcing is responsible for the highly coherent and in-phase relationship between SST and THF over the entire analyzed frequency range, although the coherence in the best-fit results is generally larger than in corresponding OBS and HR estimates. In support of this interpretation, corresponding best-fit estimates for LR (not shown) indicate that the reduced variances in OCN leads to smaller coherence and generally larger phase relative to HR. However, the best-fit estimates also reveal a stronger imprint of ocean processes than implied by the results obtained using SST and THF data from LR (Figs. 11e and 11h). While this suggest that the best-fit estimates overestimate the influence of ocean processes, the cross-spectral statistics are sensitive to the amount

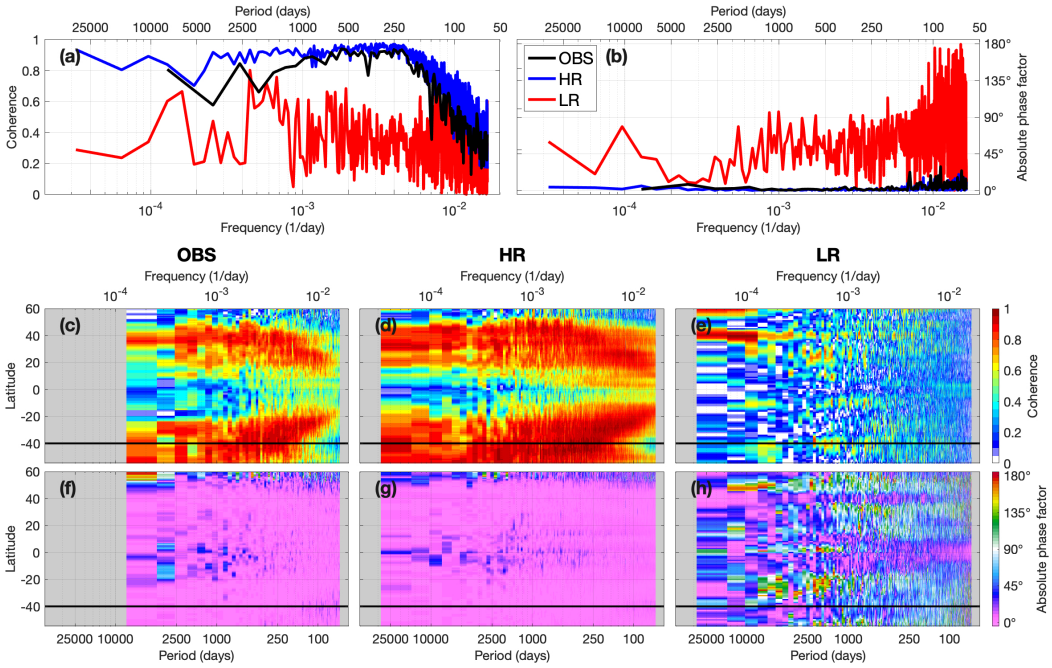

Figure 11. Similar to Fig. 6, but for coherence and absolute phase factor estimates (γ^2_{TQ} and $|\theta_{TQ}|$, respectively) computed for HR, LR, and OBS as a function of frequency (ω) for zonal wavelengths smaller than 1000 km.

of uncorrelated noise in the data. Due to simplified nature of the FCL98 stochastic model formulation defined by Eq. (6), it is possible that the best-fit results produces a larger signal-to-noise ratio than that present in the HR and LR outputs.

These results indicate that, at most extratropical latitudes, the resolved ocean variability induce a red spectrum response in frequency space in both SST and THF, and that both quantities remain highly coherent and in-phase with each other over periods from two months until the limit at the analysis at about eighty years in HR and nineteen years in OBS. The signature of ocean processes is significantly smaller in LR owing to a weaker temperature forcing by ocean processes relative to HR and OBS.

5 Discussion

5.1 Origins of the spatial-scale dependency of air-sea interactions

The results of the zonal wavenumber spectral analysis (Sec. 4.2.1) suggests that, in OBS and HR, atmospheric processes dominate the extratropical SST and THF variability and co-variability at zonal wavelengths larger than ∼2000 km while ocean processes dominate at smaller scales. Variability driven by ocean processes dominates at these

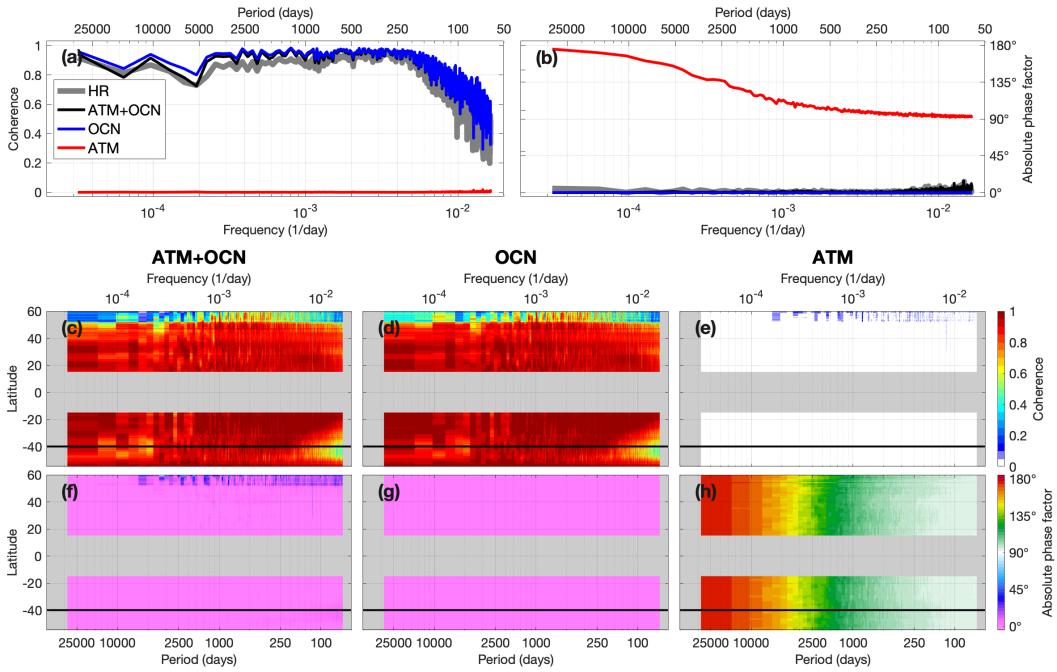

Figure 12. Similar to Fig. 8, but for best-fit stochastic model estimates of coherence and absolute phase factor ($\gamma^{2'}_{TQ}$ and $|\theta'_{TQ}|$, respectively) computed as a function of frequency (ω) for zonal wavelengths smaller than 1000 km.

scales because the atmospheric forcing spectra, while very energetic at large scales, decay toward higher wavenumbers at a steep k^{-3} rate that allows the ocean influence to become important. Supporting this interpretation, the weaker ocean forcing in LR leads to G_{TT} and G_{QQ} with shapes similar to that of the atmospheric forcing spectra.

The transition between atmosphere- to ocean-driven variability resolved by OBS and HR occurs at zonal wavelengths longer than implied by other studies. In particular, Bishop et al. (2017) computed time-domain correlations between SST tendency and THF and between SST and THF using data low-pass filtered in space using a moving average procedure (Boxcar filter), defining the transition scale as the size of the averaging window for which both pairs of quantities produce the same absolute correlations. Using satellite data, the authors obtained values smaller than 500 km in eddy-rich regions such as western boundary current systems and the ACC. The follow-up study of Small et al. (2019) investigated these relationships in an eddy-resolving climate simulation, and obtained transition scales of about 700 km at eddy-rich regions. While the differences relative to the results of the present work still need to be reconciled, they can potentially be associated with the fact that the size of the spatial averaging window does

not correspond to the filter cutoff scale. This implies that the spatial filtering operation applied in these studies potentially attenuated variability over wavelengths longer than reported, thus biasing low the estimated transition scales.

The results of the present work indicate that the influence of ocean processes becomes apparent in HR and OBS at zonal wavelengths near and below the atmospheric R_1, and the latitudinal dependence of R_1 resembles that of the scales where ocean processes start to dominate. Laurindo et al. (2019) finds a similar spatial scale dependency on the linear spectral relationship between SST and equivalent-neutral 10-m wind speed from satellite data and an eddy-resolving climate model simulation, observing negative correlations between SST and wind speed indicative of an atmosphere-driven air-sea coupling regime transitioning to positive correlations typical of an ocean-driven regime also near the atmospheric R_1. Their results relate to those of this study considering that the SST-driven anomalies in THF induce atmospheric boundary layer responses that ultimately lead to near-surface wind anomalies positively correlated with the underlying SST signal (c.f. Small et al., 2008; Chelton & Xie, 2010).

The potential physical connection between the atmospheric R_1 and the transition scale from atmosphere-driven to ocean-driven SST and THF variability warrants further investigation, although one possibility can be found at the geostrophic turbulence theory of Charney (1971). The theory predicts that the kinetic energy of synoptic-scale baroclinic atmospheric systems, that scale as a function of the Rossby radius of deformation, will be transferred to smaller spatial scales at a k^{-3} rate (Charney, 1971; Lindborg, 2006; Tulloch & Smith, 2009). Indeed, the power spectra of near-surface humidity (the quantity used to represent the atmospheric forcing signal in the FCL98 stochastic model) show a meridional variation that resembles that of the atmospheric R_1 (not shown). Since the presented results indicate that the ocean-driven SST and THF variability dominates as atmospheric motions become progressively weaker toward higher wavenumbers, the variation of the transition scale between atmosphere- and ocean-driven regimes as a function of the atmospheric R_1 is potentially underpinned by a dependence of the functional structure of the spectra of atmospheric motions on the Rossby radius of deformation.

5.2 SST and THF response to ocean forcing in frequency domain

At spatial scales smaller than 1000 km, the SST and THF variability resolved by OBS and HR show a red spectrum structure in frequency space, with both quantities remaining highly coherent and in-phase with each other over timescales from two months until the limit of the analysis at about eigthy years in HR and nineteen years in OBS at most extratropical latitudes. Corresponding stochastic model estimates (Secs. 3.2 and

719 4.2.2) suggest that these features arise from a red spectrum SST response to stochas-
720 tic ocean forcing analogous to that induced by the atmosphere (e.g., Hasselmann, 1976;
721 Frankignoul & Hasselmann, 1977), that is mirrored in THF due to the dependence of
722 this quantity on SST.

723 The stochastic model results indicate that, in HR, ocean forcing prominently en-
724 hances extratropical SST variability over periods shorter than about 500 days and shows
725 magnitudes similar to atmospheric forcing toward longer timescales, a result compati-
726 ble with the findings of Patrizio and Thompson (2021b) and Martin et al. (2021). More
727 specifically, Patrizio and Thompson (2021b) employed a stochastic climate model for-
728 mulation similar to the one used here, further accounting for a feedback term associated
729 with ocean dynamics computed as the 1-month lag-regression coefficient between OHFC
730 and SST, and found that ocean processes enhanced the temperature variability over pe-
731 riods shorter than about two years. The study by Martin et al. (2021), based on a frequency-
732 space temperature variance budget analysis of an idealized, high-resolution air-sea cou-
733 pled simulation of a western boundary current system analogous to the Gulf Stream, found
734 that the ocean dynamics prominently contributes to the upper-ocean temperature vari-
735 ability over annual timescales and shorter.

736 The influence of resolved mesoscale currents in the SST variability over a wide range
737 of timescales is also consistent with the results of Sérazin et al. (2015, 2017, 2018) and
738 Constantinou and Hogg (2021). In particular, Sérazin et al. (2015, 2018) showed that,
739 in eddy-resolving ocean-only simulations, intrinsic ocean variability dominated the SSHA
740 variance over spatial scales smaller than six geographical degrees over much of the ex-
741 tratropics at interannual to decadal timescales, also accounting for large fractions (∼30-
742 50%) of the variance over large spatial scales (>12°) at eddy-rich regions such as the ACC
743 and the seaward extensions of western boundary currents. Sérazin et al. (2017) and Constantinou
744 and Hogg (2021) found a similar influence of ocean processes in the ocean heat content
745 resolved by eddy-permitting and eddy-resolving ocean simulations.

746 The THF response to ocean-driven SST variability over a wide range of timescales
747 has been reported previously. Bishop et al. (2017) showed that the influence of internal
748 ocean dynamics in driving SST and THF anomalies increase toward lower frequencies
749 on the vicinity of energetic ocean currents, a characteristic later examined in observa-
750 tional products and in an eddy-resolving CESM simulation up to annual timescales Small
751 et al. (2019). Laurindo et al. (2019) also showed that, at zonal wavelenghts smaller than
752 ∼1000 km, satellite observations and an eddy-resolving climate simulation both resolve
753 SST variability positively-correlated with near-surface winds over periods between 10-

days and the limit of the analysis at about 2.5 years at most latitudes of all three major ocean basins.

Lastly, Gulev et al. (2013) and O'Reilly et al. (2016) reported decadal THF fluctuations driven by SST anomalies associated with the AMV (Buckley & Marshall, 2016; R. Zhang et al., 2019). Gulev et al. (2013) computed the coherence between SST and THF fluctuations inferred from historical ship-based measurements and found that they are highly coherent and approximately in-phase with each other on decadal scales. The later study of O'Reilly et al. (2016) found that this relationship was present in coupled climate simulations with active ocean dynamics but not in simulations coupled to a slab ocean. Spectral estimates obtained by the present study for the North Atlantic between 40-60°N (not shown) reveal characteristics similar to those described for the Pacific, thus supporting the conclusions of Gulev et al. (2013) and O'Reilly et al. (2016) that ocean processes can drive SST and THF variability over long timescales at the region. It is noted, however, that significant debate remains on the roles of the ocean and atmosphere in driving decadal THF fluctuations in the subpolar North Atlantic (e.g., Clement et al., 2015; R. Zhang et al., 2016; Delworth et al., 2017; Cane et al., 2017), suggesting that a dedicated analysis expanding on the methods used in this study is warranted.

5.3 Limitations of the stochastic model analysis

While the FCL98 stochastic model described by Eq. (6) can reproduce key characteristics of the extratropical SST and THF power spectra and cross-spectral statistics, it is an idealized formulation that does not represent important processes involved in thermodynamic air-sea interactions. This Section discusses such limitations and those emerging from other assumptions of the presented analysis.

First, the FCL98 stochastic model does not account for the atmospheric adjustment to SST, a process that is represented by the stochastic, coupled ocean-atmosphere energy balance model proposed by Barsugli and Battisti (1998) (hereafter BB98) employed by previous studies (Wu et al., 2006; Sura & Newman, 2008; Bishop et al., 2017; Sun & Wu, 2021). However, tests with the BB98 formulation showed that obtaining SST power spectra with magnitudes comparable to that resolved by HR and LR underestimated the THF power spectra by about two orders of magnitude. This issue potentially reflects the ocean and atmosphere becoming too strongly coupled to each other in the BB98 model, reducing the air-sea temperature contrast and consequently the THF variability. Conversely, the FCL98 model produced SST and THF power spectra with magnitudes comparable to that resolved by HR and LR, reason for which it was preferred for use in this work over the BB98 formulation.

Moreover, the FCL98 formulation used here assumes that atmospheric processes solely modulates THF by inducing stochastic variability in near-surface atmospheric temperature, thus neglecting:

(a) The role of the atmosphere on the generation of Ekman currents, which is a significant contributor to OHFC at large spatial scales (e.g., Larson et al., 2018; Small et al., 2020) and at long time-scales (Martin et al., 2021). This implies that using OHFC to represent the stochastic forcing by internal ocean processes [$\langle|\tilde{N}_o|^2\rangle$ in Eqs. (7)-(9)] potentially overestimates the ocean forcing at these scales.

(b) The atmospheric modulation of THF by the surface wind speed, factor that accounts for significant fractions of the THF variability at synoptic timescales (e.g., Alexander & Penland, 1996; Frankignoul et al., 1998; Proistosescu et al., 2018). Accounting for this effect would likely affect the stochastic model estimates of the frequency-domain THF response to atmospheric forcing, potentially leading to a higher influence of atmospheric motions over lower frequencies than implied by current results. It is noted that mesoscale SST-driven anomalies also induce anomalies in near-surface winds (c.f. Small et al., 2008; Chelton & Xie, 2010), meaning that a potential influence of this coupled response to THF are also absent in the stochastic model estimates.

(c) Radiative forcing associated with stochastic cloud variability, a process known to induce SST anomalies negatively correlated with cloud cover over seasonal timescales (e.g., Alexander et al., 2006; Spencer & Braswell, 2010; Proistosescu et al., 2018). This process can potentially also influence SST variability associated with mesoscale ocean processes, considering the observed association between mesoscale features and cloud cover (Bryan et al., 2010; Frenger et al., 2013; Desbiolles et al., 2021).

The damping of SST anomalies by upper-ocean mixing is also neglected in Eq. (6). As shown in Sec. 4.2.1, adding a diffusion term to the stochastic model formulation and assuming an eddy diffusivity coefficient κ=100 m^2/s leads to best-fit SST and THF power spectra that, at zonal wavelengths smaller than 300 km, decay at the approximate k^{-4} rate shown by corresponding HR and OBS estimates (Fig. 7). Best-fit results obtained without the diffusion effect decay at the slower k^{-2} rate, mirroring that of the OHFC data used to represent the stochastic ocean forcing. While this in principle suggests that diffusion can play a role determining the air-sea coupling characteristics at high wavenumbers, it is noted that the prescribed κ value is about one order of magnitude smaller than observational measurements (e.g. Koszalka et al., 2011; Zhurbas et al., 2014; Peng et al., 2015; Mariano et al., 2016), an underestimation that can potentially stem from the idealized nature of the FCL98 formulation. On the flip side, high-resolution, along-track

satellite SST data resolve a k^{-2} slope over wavelengths smaller than 500 km (Chin et al., 2017) – curiously similar to that of best-fit estimates without the diffusion effect. This raises the possibility that the k^{-4} slope shown by OBS and HR reflect mapping biases and/or resolution issues rather than actual geophysical characteristics (Chin et al., 2017).

Finally, this study assumes that the feedback terms α and β of Eq. (6) are constant throughout the extratropics while they in fact show significant spatial and temporal variability (e.g., Frankignoul et al., 1998; Frankignoul & Kestenare, 2002; Park et al., 2005; Patrizio & Thompson, 2021b). This limitation is partially offset by the fact that the magnitudes of the atmospheric and oceanic forcing spectra are estimated by least-squares fitting the stochastic model solutions to the SST and THF spectra resolved by HR and LR at each latitude (Appendix A). However, assuming constant coefficients can influence the frequencies where the G_{TT} and G_{QQ} response spectra becomes approximately white toward lower frequencies, and also increase the misfit between the stochastic model solutions and the reference CESM estimates.

6 Summary and conclusions

This work examines the SST and THF power spectra and cross-spectral statistics resolved by the J-OFURO3 observational product (OBS) and by multi-century climate model simulations run at eddy-parameterized and eddy-resolving ocean resolutions (LR and HR, respectively). These quantities are computed for the Pacific between 55°S and 60°N, over zonal wavelengths between ∼50 and 10000 km and periods from two months to nineteen years using OBS and eighty years using model data. The roles of atmospheric and oceanic processes in conditioning the spectral characteristics in the extratropics are interpreted using a stochastic model of the upper-ocean temperature evolution forced by noise terms representing the action of intrinsic variability in both mediums. Here, the noise terms are defined using actual geophysical data from HR and LR to simulate realistic variance distributions in spectral space.

Spectral estimates obtained as a function of zonal wavenumber indicate that, at most latitudes, all datasets resolve similar SST and THF variability at wavelengths larger than 2500 km. However, toward smaller spatial scales, their variances in HR and OBS increase relative to LR, with the most significant differences (one order of magnitude or more) found at zonal wavelengths near and smaller than the atmospheric first internal Rossby deformation radius (R_1). At these scales, SST and THF variability are highly related to each other in HR and OBS but not in LR. The corresponding stochastic model results indicate that the large-scale SST and THF variability is predominantly driven by the atmosphere and that the tight relationship between both quantities toward higher

wavenumbers in HR and OBS arise from the action of ocean processes. This relationship is virtually absent in LR due to the much weaker ocean forcing relative to HR.

The stochastic model analysis further suggests that the transition from the atmosphere-driven variability to ocean-driven in HR and OBS occurs owing to the steep k^{-3} decay of the atmosphere noise spectrum starting at zonal wavelengths larger than about 3000-4000 km. This characteristic, combined with the approximately constant (white) ocean noise spectra from the largest resolvable wavelengths until ∼300 km, allows the ocean-forced SST and THF variability to become larger than that forced by the atmosphere at scales below ∼2000 km. It is hypothesized that the similar meridional variation of the transition scale with that of the atmospheric R_1 reflects the dependence of atmospheric motions' power spectrum on the Rossby radius.

Spectral quantities computed as a function of frequency show that HR and OBS has larger SST variances than LR at most frequencies in the extratropics, most prominently over periods shorter than about 1000 days. In contrast, THF variability is enhanced relative to LR over annual periods and longer. Isolating zonal wavelengths smaller than 1000 km, HR and OBS reveal a red SST and THF power spectra (with more power over lower frequencies), with corresponding cross-spectral statistics indicating that these quantities are highly related to each other at all timescales. Corresponding stochastic model estimates suggest that these characteristics arise from the action of ocean processes. The observed red spectral response in SST to ocean forcing is analogous to that induced by stochastic atmospheric variability, where the ocean integrates the noise to induce low-frequency oscillations. This red spectrum response is also seen in THF due to the dependence of this quantity on SST.

These results support the conclusion that climate models with eddy-resolving oceans resolve more realistic air-sea coupling characteristics than their eddy-parameterized counterparts. In particular, they indicate that resolved mesoscale ocean phenomena can modulate a significant fraction of the extratropical SST and THF variability over a wide range of spatial scales [$\mathcal{O}(10^1$-10^3 km)] and from intraseasonal to multidecadal timescales. Finally, it is noted that, while stochastic models can be used to infer the roles of the atmosphere and ocean in driving SST and THF variability, these idealized systems cannot represent all the physical complexity of the processes involved in the thermodynamic air-sea interactions, nor inform about the nature of the phenomena in both mediums responsible for the generation and dissipation of SST anomalies. With this in mind, a potential follow-on investigation involves using spectral methods to examine the key terms in the upper-ocean heat balance equation and in the turbulent heat flux bulk formula-

tions responsible for maintaining the SST and THF variability over different spatial and temporal scales across the global ocean, as resolved by high-resolution climate models.

Acknowledgments

This research was supported in part by the National Center for Atmospheric Research (NCAR), which is a major facility sponsored by the National Science Foundation (NSF) under Cooperative Agreement No. 1852977; and in part by the International Laboratory for High Resolution Earth System Prediction (iHESP), a collaboration between the Qingdao National Laboratory for Marine Science and Technology (QNLM), Texas A&M University (TAMU), and NCAR. L. Siqueira and B. Kirtman acknowledge support from NSF (OCE1419569, OCE1559151), the National Oceanic and Atmospheric Administration (NOAA, NA18OAR4310293, NA15OAR4320064), and the U.S. Department of Energy (DOE, DE-SC0019433). P. Chang acknowledge support from NSF (AGS1462127), NOAA (NA20OAR4310409), and DOE (DE-SC0020072). The outputs from the HR climate model simulation used in this study are distributed by iHESP at `https://ihesp.tamu.edu/products/ihesp-products/data-release/PI_control/index.html` – the LR version of this dataset will be publicly released soon. The J-OFURO3 data can be obtained at `https://j-ofuro.isee.nagoya-u.ac.jp/en/dataset/entry-323.html`, the Chelton et al. (1998) global climatology of the oceanic first internal Rossby radius of deformation (R_1) is available at `https://ceoas.oregonstate.edu/rossby_radius`, and the NCEP reanalysis model data used to compute the atmospheric R_1 is available at `https://psl.noaa.gov/data/gridded/data.ncep.reanalysis.html`. The data analyses were carried out using computing resources provided by the Texas A&M High Performance Research Computing and by the Climate Simulation Laboratory at NCAR's Computational and Information Systems Laboratory. L. Laurindo, R. Small, and F. Bryan gratefully acknowledge Stuart Bishop, Patrizio Casey, and Yiming Guo for very helpful discussions throughout the development of this work. The authors also thank Claude Frankignoul for his feedback on an early version of this manuscript.

Appendix A Approximating the stochastic model solutions to HR and LR estimates

This work estimates the variances σ_o^2 and σ_a^2 that the forcing spectra $\langle|\tilde{N}_o|^2\rangle$ and $\langle|\tilde{N}_a|^2\rangle$ should integrate to for approximating the stochastic model solutions to the SST and THF power spectra and cross-spectral statistics resolved by HR and LR. This is done by least-squares fitting the G_{TT} and G_{QQ} analytical solutions [Eqs. (7)-(8)] to the SST and THF spectra resolved by the CESM simulations.

First, these expressions are rewritten as:

$$G_{TT}(k,\omega,j) = \left\{ \frac{2\nu^2|\tilde{N}_o(k,\omega,j)|^2}{l_k l_\omega \left[4\pi^2\omega^2 + (\alpha+\beta)^2\right]} \right\} \sigma_o^2 + \left\{ \frac{2\alpha^2|\tilde{N}_a(k,\omega,j)|^2}{l_k l_\omega \left[4\pi^2\omega^2 + (\alpha+\beta)^2\right]} \right\} \sigma_a^2, \tag{A1}$$

$$G_{QQ}(k,\omega,j) = \left\{ \frac{2\lambda_q^2\nu^2|\tilde{N}_o(k,\omega,j)|^2}{l_k l_\omega \left[4\pi^2\omega^2 + (\alpha+\beta)^2\right]} \right\} \sigma_o^2 + \left\{ \frac{2\lambda_q^2(4\pi^2\omega^2+\beta^2)|\tilde{N}_a(k,\omega,j)|^2}{l_k l_\omega \left[4\pi^2\omega^2 + (\alpha+\beta)^2\right]} \right\} \sigma_a^2. \tag{A2}$$

where j = 1, 2, 3, ..., n_j denotes the number of individual $|\tilde{N}_o|^2$ and $|\tilde{N}_a|^2$ estimates available at each latitude (equal to 48 for HR and 44 for LR).

Using known $G_{TT}(k,\omega,j)$, $G_{QQ}(k,\omega,j)$, $|\tilde{N}_o(k,\omega,j)|^2$, and $|\tilde{N}_a(k,\omega,j)|^2$ (defined using HR and LR data following the methods described in Sec. 2), σ_o^2 and σ_a^2 can then be estimated via least-squares. Prior to the fitting operation, these spectra are randomly matched without replacement (i.e., shuffled) along the j dimension to reduce correlations arising the zonal and temporal coincidence of the data.

Considering n_k (n_ω) as the number of discrete coordinates in k (ω), Eqs. (A1) and (A2) are then redefined as a system with $n = 2n_k n_\omega n_j$ linear equations, as:

$$y_i = A_i\sigma_o^2 + B_i\sigma_a^2, \tag{A3}$$

where i = 1, 2, 3, ..., n. Here, y_i holds the G_{TT} and G_{QQ} estimates, A_i and B_i are the terms enclosed by braces dependent on $|\tilde{N}_o|^2$ and $|\tilde{N}_a|^2$, respectively, and σ_o^2 and σ_a^2 are the unknowns of the system.

In matrix form, Eq. (A3) can be rewritten as $y = Mz$, where M is an $n\times2$ matrix containing the A and B vectors, and z is an 2×1 column vector with the unknowns σ_a^2 and σ_o^2. A least-squares solution for z can then be computed as:

$$z = (M^{\mathrm{T}}M)^{-1}(M^{\mathrm{T}}y), \tag{A4}$$

where the superscript "T" denotes transposed matrices.

References

Alexander, M. A., & Penland, C. (1996). Variability in a mixed layer ocean model driven by stochastic atmospheric forcing. *Journal of Climate*, *9*(10), 2424–2442. doi: https://doi.org/10.1175/1520-0442(1996)009⟨2424:VIAMLO⟩2.0.CO;2

Alexander, M. A., Yin, J., Branstator, G., Capotondi, A., Cassou, C., Cullather, R., ... Wainer, I. (2006). Extratropical atmosphere–ocean variability in CCSM3. *Journal of Climate*, *19*(11), 2496–2525. doi: https://doi.org/10.1175/JCLI3743.1

Barsugli, J. J., & Battisti, D. S. (1998). The basic effects of atmosphere–ocean thermal coupling on midlatitude variability. *Journal of Atmospheric Sciences*, *55*(4), 477–493. doi: https://doi.org/10.1175/1520-0469(1998)055⟨0477:TBEOAO⟩2.0.CO;2

Bendat, J. S., & Piersol, A. G. (1986). *Random Data: Analysis and Measurement Procedures* (3rd ed.). John Wiley & Sons, Inc. (594 pp.) doi: https://doi.org/10.1002/9781118032428

Berloff, P., & Kamenkovich, I. (2013a). On the spectral analysis of mesoscale eddies. Part II: Nonlinear analysis. *Journal of Physical Oceanography*, *43*, 2528-2544. doi: https://doi.org/10.1175/JPO-D-12-0233.1

Berloff, P., & Kamenkovich, I. (2013b). On the spectral analysis of mesoscale eddies. Part I: Linear analysis. *Journal of Physical Oceanography*, *43*, 2505-2527. doi: https://doi.org/10.1175/JPO-D-12-0232.1

Bishop, S. P., Small, R. J., Bryan, F. O., & Tomas, R. A. (2017). Scale dependence of midlatitude air-sea interaction. *Journal of Climate*, *30*, 8207–8221. doi: https://doi.org/10.1175/JCLI-D-17-0159.1

Bryan, F. O., Tomas, R., Dennis, J. M., Chelton, D. B., Loeb, N. G., & McClean, J. L. (2010). Frontal scale air–sea interaction in high-resolution coupled climate models. *Journal of Climate*, *23*, 6277–6291. doi: https://doi.org/10.1175/2010JCLI3665.1

Buckley, M. W., & Marshall, J. (2016). Observations, inferences, and mechanisms of the Atlantic Meridional Overturning Circulation: A review. *Reviews of Geophysics*, *54*(1), 5–63. doi: https://doi.org/10.1002/2015RG000493

Buckley, M. W., Ponte, R. M., Forget, G., & Heimbach, P. (2015). Determining the origins of advective heat transport convergence variability in the North Atlantic. *Journal of Climate*, *28*(10), 3943–3956. doi: https://doi.org/10.1175/JCLI-D-14-00579.1

Callies, J., Ferrari, R., & Bühler, O. (2014). Transition from geostrophic turbulence to inertia–gravity waves in the atmospheric energy spectrum. *Proceedings of the National Academy of Sciences of the United States of America*, *111*(48), 17033–17038. doi: https://doi.org/10.1073/pnas.1410772111

Cane, M. A., Clement, A. C., Murphy, L. N., & Bellomo, K. (2017). Low-pass filtering, heat flux, and Atlantic Multidecadal Variability. *Journal of Climate*,

30(18), 7529–7553. doi: https://doi.org/10.1175/JCLI-D-16-0810.1

Chang, P., Zhang, S., Danabasoglu, G., Yeager, S. G., Fu, H., Wang, H., ... Wu, L. (2020). An unprecedented set of high-resolution earth system simulations for understanding multiscale interactions in climate variability and change. *Journal of Advances in Modeling Earth System*, *12*(12), e2020MS002298. doi: https://doi.org/10.1029/2020MS002298

Charney, J. G. (1971). Geostrophic turbulence. *Journal of Atmospheric Sciences*, *28*, 1087–1095. doi: https://doi.org/10.1175/1520-0469(1971)028⟨1087:GT⟩2.0.CO;2

Chelton, D. B., deSzoeke, R. A., Schlax, M. G., Naggar, K. E., & Siwertz, N. (1998). Geographical variability of the first baroclinic rossby radius of deformation. *Journal of Physical Oceanography*, *28*(3), 433 - 460. doi: https://doi.org/10.1175/1520-0485(1998)028⟨0433:GVOTFB⟩2.0.CO;2

Chelton, D. B., Gaube, P., Schlax, M. G., Early, J. J., & Samelson, R. M. (2011). The influence of nonlinear mesoscale eddies on near-surface oceanic chlorophyll. *Science*, *334*, 328–332. doi: https://doi.org/10.1126/science.1208897

Chelton, D. B., Schlax, M. G., Freilich, M. H., & Milliff, R. F. (2004). Satellite measurements reveal persistent small-scale features in ocean winds. *Science*, *303*, 978–983. doi: https://doi.org/10.1126/science.1091901

Chelton, D. B., Schlax, M. G., & Samelson, R. M. (2011). Global observation of nonlinear mesoscale eddies. *Progress in Oceanography*, *91*(2), 167–216. doi: https://doi.org/10.1016/j.pocean.2011.01.002

Chelton, D. B., & Xie, S.-P. (2010). Coupled ocean-atmosphere interaction at the oceanic mesoscale. *Oceanography*, *23*(4), 52–62. doi: https://doi.org/10.5670/oceanog.2010.05

Chin, T. M., Vazquez-Cuervo, J., & Armstrong, E. M. (2017). A multi-scale high-resolution analysis of global sea surface temperature. *Remote Sensing of Environment*, *200*, 154–169. doi: https://doi.org/10.1016/j.rse.2017.07.029

Cho, J. Y. N., Zhu, Y., Newell, R. E., Anderson, B. E., Barrick, J. D., Gregory, G. L., ... Albercook, G. M. (1999). Horizontal wavenumber spectra of winds, temperature, and trace gases during the Pacific Exploratory Missions: 1. Climatology. *Journal of Geophysical Research*, *104*(D5), 5697–5716. doi: https://doi.org/10.1029/98JD01825

Clement, A., Bellomo, K., Murphy, L. N., Cane, M. A., Mauritsen, T., Rädel, G., & Stevens, B. (2015). The Atlantic Multidecadal Oscillation without a role for ocean circulation. *Science*, *350*(6258), 320–324. doi: https://doi.org/10.1126/science.aab3980

Constantinou, N. C., & Hogg, A. M. (2021). Intrinsic oceanic decadal variability of upper-ocean heat content. *Journal of Climate*, 1–41. (published online) doi: https://doi.org/10.1175/JCLI-D-20-0962.1

Danabasoglu, G., Bates, S. C., Briegleb, B. P., Jayne, S. R., Jochum, M., Large, W. G., ... Yeager, S. G. (2012). The CCSM4 ocean component. *Journal of Climate*, *25*(5), 1361–1389. doi: https://doi.org/10.1175/JCLI-D-11-00091.1

Delworth, T. L., Zeng, F., Zhang, L., Zhang, R., Vecchi, G. A., & Yang, X. (2017). The central role of ocean dynamics in connecting the North Atlantic Oscillation to the extratropical component of the Atlantic Multidecadal Oscillation. *Journal of Climate*, *30*(10), 3789—3805. doi: https://doi.org/10.1175/JCLI-D-16-0358.1

Desbiolles, F., Alberti, M., Hamouda, M. E., Meroni, A. N., & Pasquero, C. (2021). Links between sea surface temperature structures, clouds and rainfall: Study case of the Mediterranean Sea. *Geophysical Research Letters*, *48*, e2020GL091839. doi: https://doi.org/10.1029/2020GL091839

Ducet, N., Le Traon, P.-Y., & Reverdin, G. (2000). Global high-resolution mapping of ocean circulation from TOPEX/Poseidon and ERS-1 and -2. *Journal of Geophysical Research*, *105*(C8), 19,477-19,498. doi: https://doi.org/10.1029/2000JC900063

Early, J. J., Samelson, R. M., & Chelton, D. B. (2011). The evolution and propagation of quasigeostrophic ocean eddies. *Journal of Physical Oceanography*, *41*, 1535–1555. doi: https://doi.org/10.1175/2011JPO4601.1

Fairall, C. W., Bradley, E. F., Hare, J. E., Grachev, A. A., & Edson, J. B. (2003). Bulk parameterization of air-sea fluxes: updates and verification for the COARE algorithm. *Journal of Climate*, *16*, 571—591. doi: https://doi.org/10.1175/1520-0442(2003)016⟨0571:BPOASF⟩2.0.CO;2

Frankignoul, C., Czaja, A., & L'Heveder, B. (1998). Air-sea feedback in the North Atlantic and surface boundary conditions for ocean models. *Journal of Climate*, *11*, 2310—2324. doi: https://doi.org/10.1175/1520-0442(1998)011⟨2310:ASFITN⟩2.0.CO;2

Frankignoul, C., & Hasselmann, K. (1977). Stochastic climate models, Part II Application to sea-surface temperature anomalies and thermocline variability. *Tellus*, *29*(4), 289—305. doi: https://doi.org/10.3402/tellusa.v29i4.11362

Frankignoul, C., & Kestenare, E. (2002). The surface heat flux feedback. Part I: estimates from observations in the Atlantic and the North Pacific. *Climate Dynamics*, *19*(8), 633–647. doi: https://doi.org/10.1007/s00382-002-0252-x

Frenger, I., Gruber, N., Knutti, R., & Münnich, M. (2013). Imprint of Southern

Ocean eddies on winds, clouds and rainfall. *Nature Geoscience*, *6*, 608–612. doi: https://doi.org/10.1038/NGEO1863

Gaube, P., Chelton, D., Samelson, R. M., Schlax, M. G., & O'Neill, L. W. (2015). Satellite observations of mesoscale eddy-induced Ekman pumping. *Journal of Physical Oceanography*, *45*, 104–132. doi: https://doi.org/10.1175/JPO-D-14-0032.1

Gent, P. R., & McWilliams, J. C. (1990). Isopycnal mixing in ocean circulation models. *Journal of Physical Oceanography*, *20*(1), 150–155. doi: https://doi.org/10.1175/1520-0485(1990)020⟨0150:IMIOCM⟩2.0.CO;2

Gulev, S. K., Latif, M., Keenlyside, N., Park, W., & Koltermann, K. P. (2013). North Atlantic Ocean control on surface heat flux on multidecadal timescales. *Nature*, *499*(7459), 464-467. doi: https://doi.org/10.1038/nature12268

Hasselmann, K. (1976). Stochastic climate models Part I. Theory. *Tellus*, *28*(6), 473–485. doi: https://doi.org/10.1111/j.2153-3490.1976.tb00696.x

Hunke, E. C., & Lipscomb, W. H. (2010). *CICE: the Los Alamos Sea Ice Model Documentation and Software User's Manual Version 4.1.* Los Alamos os Alamos National Laboratory Tech. Rep. 87545. (76 pp.)

Kalnay, E., Kanamitsu, M., Kistler, R., Collins, W., Deaven, D., Gandin, L., ... Joseph, D. (1996). The NCEP/NCAR 40-Year Reanalysis Project. *Bulletin of the American Meteorological Society*, *77*(3), 437-471. doi: 10.1175/1520-0477(1996)077⟨0437:TNYRP⟩2.0.CO;2

Kirtman, B. P., Bitz, C., Bryan, F., Collins, W., Dennis, J., Hearn, N., ... Vertenstein, M. (2012). Impact of ocean model resolution on CCSM climate simulations. *Climate Dynamics*, *39*, 1303–1328. doi: https://doi.org/10.1007/s00382-012-1500-3

Kirtman, B. P., Perlin, N., & Siqueira, L. (2017). Ocean eddies and climate predictability. *Chaos*, *27*(12), 126902. doi: https://doi.org/10.1063/1.4990034

Koszalka, I., LaCasce, J. H., Andersson, M., Orvik, K. A., & Mauritzen, C. (2011). Surface circulation in the Nordic Seas from clustered drifters. *Deep-Sea Research I*, *58*, 468–485. doi: https://doi.org/10.1016/j.dsr.2011.01.007

Kubota, M., Iwasaka, N., Kizu, S., Konda, M., & Kutsuwada, K. (2002). Japanese ocean flux data sets with use of remote sensig observations (J-OFURO). *Journal of Oceanography*, *58*, 213—225. doi: https://doi.org/10.1023/A:1015845321836

Large, W. G., & Yeager, S. G. (2004). *Diurnal to decadal global forcing for ocean and sea-ice models: the data sets and flux climatologies.* NCAR technical note NCAR/TN-460+STR. (`https://doi.org/10.5065/D6KK98Q6`)

Larson, S. M., Vimont, D. J., Clement, A. C., & Kirtman, B. P. (2018). How momentum coupling affects SST variance and large-scale Pacific climate variability in CESM. *Journal of Climate*, *31*(7), 2927–2944. doi: https://doi.org/10.1175/JCLI-D-17-0645.1

Laurindo, L. C., Siqueira, L., Mariano, A. J., & Kirtman, B. P. (2019). Cross-spectral analysis of the SST/10-m wind speed coupling resolved by satellite products and climate model simulations. *Climate Dynamics*, *52*(9), 5071—5098. doi: https://doi.org/10.1007/s00382-018-4434-6

Lawrence, D. M., Oleson, K. W., Flanner, M. G., Thornton, P. E., Swenson, S. C., Lawrence, P. J., ... Slater, A. G. (2011). Parameterization improvements and functional and structural advances in Version 4 of the Community Land Model. *Journal of Advances in Modeling Earth System*, *3*(1). doi: https://doi.org/10.1029/2011MS000045

Lindborg, E. (2006). The energy cascade in a strongly stratified fluid. *Journal of Fluid Mechanics*, *550*, 207–242. doi: https://doi.org/10.1017/S0022112005008128

Ma, X., Chang, P., Saravanan, R., Montuoro, R., Hsieh, J.-S., Wu, D., ... Jing, Z. (2015). Distant influence of Kuroshio eddies on North Pacific weather patterns? *Scientific Reports*, *5*, 17785. doi: https://doi.org/10.1038/srep17785

Ma, X., Chang, P., Saravanan, R., Montuoro, R., Nakamura, H., Wu, D., ... Wu, L. (2017). Importance of resolving Kuroshio front and eddy influence in simulating the North Pacific storm track. *Journal of Climate*, *30*, 1861–1880. doi: https://doi.org/10.1175/JCLI-D-16-0154.1

Ma, X., Jing, Z., Chang, P., Liu, X., Montuoro, R., Small, R. J., ... Wu, L. (2016). Western boundary currents regulated by interaction between ocean eddies and the atmosphere. *Nature*, *535*, 533–537. doi: https://doi.org/10.1038/nature18640

Mahajan, S., Saravanan, R., & Chang, P. (2009). The role of the wind-evaporation-sea surface temperature (WES) feedback in air–sea coupled tropical variability. *Atmospheric Research*, *94*(1), 19–36. doi: https://doi.org/10.1016/j.atmosres.2008.09.017

Mariano, A. J., Ryan, E. H., Huntley, H. S., Laurindo, L., Coelho, E., Griffa, A., ... Wei, M. (2016). Statistical properties of the surface velocity field in the northern Gulf of Mexico sampled by GLAD drifters. *Journal of Geophysical Research: Oceans*, *121*(7), 5193–5216. doi: https://doi.org/10.1002/2015JC011569

Martin, P. E., Arbic, B. K., & Hogg, A. M. (2021). Drivers of atmospheric and

oceanic surface temperature variance: A frequency domain approach. *Journal of Climate*, *34*(10), 3975–3990. doi: https://doi.org/10.1175/JCLI-D-20-0557.1

Meehl, G. A., Yang, D., Arblaster, J. M., Bates, S. C., Rosenbloom, N., Neale, R., ... Danabasoglu, G. (2019). Effects of model resolution, physics, and coupling on southern hemisphere storm tracks in CESM1.3. *Geophysical Research Letters*, *46*(21), 12408-12416. doi: https://doi.org/10.1029/2019GL084057

Minobe, S., Kuwano-Yoshida, A., Komori, N., Xie, S.-P., & Small, R. J. (2008). Influence of the Gulf Stream on the troposphere. *Nature*, *452*, 206–209. doi: https://doi.org/10.1038/nature06690

Nastrom, G. D., & Gage, K. S. (1985). A climatology of atmospheric wavenumber spectra of wind and temperature observed by commercial aircraft. *Journal of Atmospheric Sciences*, *42*(9), 950–960. doi: https://doi.org/10.1175/1520-0469(1985)042⟨0950:ACOAWS⟩2.0.CO;2

Neale, R. B., Gettelman, A., Park, S., Chen, C.-C., Lauritzen, P. H., Williamson, D. L., ... Taylor, M. A. (2012). *Description of the NCAR Community Atmosphere Model (CAM 5.0).* NCAR TECHNICAL NOTE NCAR/TN-486+STR. (289 pp.)

O'Brien, R. C., Cipollini, P., & Blundell, J. R. (2013). Manifestation of oceanic Rossby waves in long-term multiparametric satellite datasets. *Remote Sensing of Environment*, *129*, 111-121. doi: https://doi.org/10.1016/j.rse.2012.10.024

Okumura, Y., Xie, S.-P., Numaguti, A., & Tanimoto, Y. (2001). Tropical Atlantic air-sea interaction and its influence on the NAO. *Geophysical Research Letters*, *28*(8), 1507–1510. doi: https://doi.org/10.1029/2000GL012565

O'Neill, L. W., Chelton, D. B., & Esbensen, S. K. (2010). The effects of SST-induced surface wind speed and direction gradients on midlatitude surface vorticity and divergence. *Journal of Climate*, *23*, 255–281. doi: https://doi.org/10.1175/2009JCLI2613.1

O'Reilly, C. H., Huber, M., Woollings, T., & Zanna, L. (2016). The signature of low-frequency oceanic forcing in the Atlantic Multidecadal Oscillation. *Geophysical Research Letters*, *43*(6), 2810–2818. doi: https://doi.org/10.1002/2016GL067925

Park, S., Deser, C., & Alexander, M. A. (2005). Estimation of the surface heat flux response to sea surface temperature anomalies over the global oceans. *Journal of Climate*, *18*(21), 4582–4599. doi: https://journals.ametsoc.org/view/journals/clim/18/21/jcli3521.1.xml

Patrizio, C. R., & Thompson, D. W. J. (2021a). Quantifying the role of ocean

dynamics in ocean mixed layer temperature variability. *Journal of Climate*, *34*(7), 2567–2589. doi: https://doi.org/10.1175/JCLI-D-20-0476.1

Patrizio, C. R., & Thompson, D. W. J. (2021b). Understanding the Role of Ocean Dynamics in Midlatitude Sea Surface Temperature Variability using a Simple Climate Model. *Journal of Climate*. (Submitted)

Peng, S., Qian, Y.-K., Lumpkin, R., Li, P., Wang, D., & Du, Y. (2015). Characteristics of the near-surface currents in the Indian Ocean as deduced from satellite-tracked surface drifters. Part II: Lagrangian statistics. *Journal of Physical Oceanography*, *45*(2), 459–477. doi: https://doi.org/10.1175/JPO-D-14-0049.1

Polito, P. S., & Sato, O. T. (2015). Do eddies ride on Rossby waves? *Journal of Geophysical Research: Oceans*, *120*, 5417–5435. doi: https://doi.org/10.1002/2015JC010737

Proistosescu, C., Donohoe, A., Armour, K. C., Roe, G. H., Stuecker, M. F., & Bitz, C. M. (2018). Radiative feedbacks from stochastic variability in surface temperature and radiative imbalance. *Geophysical Research Letters*, *45*(10), 5082–5094. doi: https://doi.org/10.1029/2018GL077678

Putrasahan, D. A., Kamenkovich, I., Le Hénaff, M., & Kirtman, B. P. (2017). Importance of ocean mesoscale variability for air-sea interactions in the Gulf of Mexico. *Geophysical Research Letters*, *44*, 6352–6362. doi: https://doi.org/10.1002/2017GL072884

Putrasahan, D. A., Miller, A., & Seo, H. (2013). Isolating mesoscale coupled ocean–atmosphere interactions in the Kuroshio Extension region. *Dynamics of Atmospheres and Oceans*, *63*, 60–78. doi: https://doi.org/10.1016/j.dynatmoce.2013.04.001

Roberts, M. J., Hewitt, H. T., Hyder, P., Ferreira, D., Josey, S. A., Mizielinski, M., & Shelly, A. (2016). Impact of ocean resolution on coupled air-sea fluxes and large-scale climate. *Geophysical Research Letters*, *43*(19), 10430–10438. doi: https://doi.org/10.1002/2016GL070559

Siqueira, L., & Kirtman, B. (2016). Atlantic near-term climate variability and the role of a resolved Gulf Stream. *Geophysical Research Letters*, *43*, 3964—3972. doi: https://doi.org/10.1002/2016GL068694

Siqueira, L., Kirtman, B., & Laurindo, L. C. (2021). Forecasting remote atmospheric responses to decadal Kuroshio stability transitions. *Journal of Climate*, *34*(1), 379–395. doi: https://doi.org/10.1175/JCLI-D-20-0139.1

Small, R. J., Bryan, F. O., Bishop, S. P., Larson, S., & Tomas, R. A. (2020). What drives upper-ocean temperature variability in coupled climate models and ob-

servations. *Journal of Climate*, *33*, 577—596. doi: https://doi.org/10.1175/JCLI-D-19-0295.1

Small, R. J., Bryan, F. O., Bishop, S. P., & Tomas, R. A. (2019). Air–sea turbulent heat fluxes in climate models and observational analyses: What drives their variability? *Journal of Climate*, *32*(8), 2397—2421. doi: https://doi.org/10.1175/JCLI-D-18-0576.1

Small, R. J., deSzoeke, S. P., Xie, S.-P., O'Neill, L., Seo, H., Song, Q., ... Minobe, S. (2008). Air-sea interaction over ocean fronts and eddies. *Dynamics of Atmospheres and Oceans*, *45*, 274–319. doi: https://doi.org/10.1016/j.dynatmoce.2008.01.001

Smith, R., Jones, P., Briegleb, B., Bryan, F., Danabasoglu, G., Dennis, J., ... Yeager, S. (2010). *The Parallel Ocean Program (POP) Reference Manual.* Los Alamos National Laboratory Tech. Rep. LAUR-10-01853. (141 pp.)

Spencer, R. W., & Braswell, W. D. (2010). On the diagnosis of radiative feedback in the presence of unknown radiative forcing. *Journal of Geophysical Research*, *115*(D16), D16109. doi: https://doi.org/10.1029/2009JD013371

Sun, X., & Wu, R. (2021). Seasonality and time scale dependence of the relationship between turbulent surface heat flux and SST. *Journal of Climate*. doi: https://doi.org/10.1007/s00382-021-05631-0

Sura, P., & Newman, M. (2008). The impact of rapid wind variability upon air–sea thermal coupling. *Journal of Climate*, *21*, 621—637. doi: https://doi.org/10.1175/2007JCLI1708.1

Sérazin, G., Jaymond, A., Leroux, S., Penduff, T., Bessières, L., Llovel, W., ... Terray, L. (2017). A global probabilistic study of the ocean heat content low-frequency variability: Atmospheric forcing versus oceanic chaos. *Geophysical Research Letters*, *44*(11), 5580–5589. doi: https://doi.org/10.1002/2017GL073026

Sérazin, G., Penduff, T., Barnier, B., Molines, J.-M., Arbic, B. K., Müller, M., & Terray, L. (2018). Inverse cascades of kinetic energy as a source of intrinsic variability: A global ogcm study. *Journal of Physical Oceanography*, *48*(6), 1385–1408. doi: https://doi.org/10.1175/JPO-D-17-0136.1

Sérazin, G., Penduff, T., Grégorio, S., Barnier, B., Molines, J.-M., & Terray, L. (2015). Intrinsic variability of sea level from global ocean simulations: Spatiotemporal scale. *Journal of Climate*, *28*(10), 4279–4292. doi: https://doi.org/10.1175/JCLI-D-14-00554.1

Tomita, H., Hihara, T., Kako, S., Kubota, M., & Kutsuwada, K. (2019). An introduction to J-OFURO3, a third-generation Japanese ocean flux data set using

remote-sensing observations. *Journal of Oceanography*, *75*, 71—194. doi: https://doi.org/10.1007/s10872-018-0493-x

Tulloch, R., & Smith, K. S. (2009). Quasigeostrophic turbulence with explicit surface dynamics: application to the atmospheric energy spectrum. *Journal of Atmospheric Sciences*, *66*, 450–467. doi: https://doi.org/10.1175/2008JAS2653.1

Villas Bôas, A. B., Sato, O. T., Chaigneau, A., & Castelão, G. P. (2015). The signature of mesoscale eddies on the air-sea turbulent heat fluxes in the South Atlantic Ocean. *Geophysical Research Letters*, *42*, 1856-1862. doi: https://doi.org/10.1002/2015GL063105

von Storch, J.-S. (2000). Signatures of air–sea interactions in a coupled atmosphere–ocean GCM. *Journal of Climate*, *13*(19), 3361—3379. doi: https://doi.org/10.1175/1520-0442(2000)013⟨3361:SOASII⟩2.0.CO;2

Wu, R., Kirtman, B. P., & Pegion, K. (2006). Local air–sea relationship in observations and model simulations. *Journal of Climate*, *19*, 4914—4932. doi: https://doi.org/10.1175/JCLI3904.1

Xie, S.-P. (2004). Satellite observations of cool ocean-atmosphere interaction. *Bulletin of the American Meteorological Society*, *85*(2), 195–208. doi: https://doi.org/10.1175/BAMS-85-2-195

Zhang, R., Sutton, R., Danabasoglu, G., Delworth, T. L., Kim, W. M., Robson, J., & Yeager, S. G. (2016). Comment on "The Atlantic Multidecadal Oscillation without a role for ocean circulation". *Science*, *352*(6293), 1527–1527. doi: https://doi.org/10.1126/science.aaf1660

Zhang, R., Sutton, R., Danabasoglu, G., Kwon, Y.-O., Marsh, R., Yeager, S. G., ... Little, C. M. (2019). A review of the role of the Atlantic Meridional Overturning Circulation in Atlantic Multidecadal Variability and associated climate impacts. *Reviews of Geophysics*, *57*(2), 316—375. doi: https://doi.org/10.1029/2019RG000644

Zhang, S., Fu, H., Wu, L., Li, Y., Wang, H., Zeng, Y., ... Guo, Y. (2020). Optimizing high-resolution community earth system model on a heterogeneous many-core supercomputing platform. *Geoscientific Model Development*, *13*(10), 4809–4829. doi: https://doi.org/10.5194/gmd-13-4809-2020

Zhurbas, V., Lyzhkov, D., & Kuzmina, N. (2014). Drifter-derived estimates of lateral eddy diffusivity in the World Ocean with emphasis on the Indian Ocean and problems of parameterisation. *Deep-Sea Research I*, *83*, 1–11. doi: https://doi.org/10.1016/j.dsr.2013.09.001